

Dear colleague,

It seems that it is not possible to keep the italic-blue color formatting we used in our answers to recall your comments. You will find as a supplement a pdf file that gathers our comments and the proposed revised version of our work.

First, we want to thank you for your editorial works. We have taken into account or try to answer positively to all of your comments concerning the opportunity to publish the new code; the discussion and interpretation of the results and the revisions of text. Following your advices several parts of the paper have been rewritten, several figures have been modified and new explanations have been added to better justify or improve results presentations. In particular, we followed your suggestion, presenting the temperature patterns obtained for the various accretion geometries as differences to those of the Gabbro Glacier "G" structure. We also clarified in the text and in the new version of Fig. 5 the difference between the instantaneous and average cooling rates that are obtained from the time evolution of tracers along trajectories within the crust with cooling rates obtained by petrologists. In the new version of the paper, all the references to the petrological results have been shift and clearly separated from the numerical model results. We suppress all the reference to "Igneous Cooling Rate, ICR" or "Subsolidus Cooling Rate, SCR" describing our results to emphasize on the average cooling rate that are obtained and are not comparable with the petrological ones without cautions. This is why Fig. 6 has been joined to the section describing the numerical results and received new labels. We have improved the discussion to take these restrictions into account. You will find below the detailed answers for each of your comments, which are recalled in blue italic. Thanking you again, for the help you brought us improving the scientific content of our paper, we hope that this new version will find your approbation for publication.

Sincerely yours,

Philippe Machetel and Carlos Garrido

Global comments:

Overall I consider that the manuscript requires minor revisions, because it could present interesting results on the thermal evolution of crustal accretion in mid-ocean ridges, provided that some changes are made before publication. The numerical model with its strengths and limitations has been developed in previous studies. In my opinion, a more robust argumentation is required to justify some rather arbitrary choices in the model setup and interpretation of the results (for example, variation of Φ with depth, viscosity of the crust, melting vs temperature, discussion on cooling rates).

This work depicts significant improvements of our computing tool devoted to the exploration of the thermal and dynamic effects for mid-oceanic ridge studies. However, in spite of their common properties, each ridge is also a particular case, with its own local properties and configurations. This complicates the choice of particular physical values and justifies their large parametric explorations. These needs are emphasized by the open scientific debates that exist among the scientific community about the structure of the ridge itself, the location or the strength of the hydrothermal

cooling. These debates are still open for the cracking temperature values, the viscosity contrast in the upper crust but also for the importance of the feedbacks between uncertainties on these variables. Our program has been designed to allow broad, easy (and quite cheap in term of computer time - from a few hours to a few days on modern PC) explorations of these assumptions. This should be considered as an advantage able to bring large possibilities of parameter explorations to who it may be interested. However, it also presents the difficulty of synthetic presentations of numerous crossed possible explorations and cases. The aim of the current paper is not presenting exhaustive explorations of these free parameters, but to present some cases exploring the effects on results of intrusion geometry, hydrothermal cooling location and amplitude, cracking temperature and viscosity. This work illustrates the possibilities of the new version of the code with broadly accepted geophysical parameter values, knowing that the source (Fortran code) and the data files are easy to modify to customize the parameter to explor.

New explanations have been added in the introduction and in the abstract of the paper to clarify these points and references have been added and/or modified in the text to justify the choices for crystallization curve, viscosity and cracking temperature hypotheses.

Section 5 (thermal history and cooling of the lower crust) should be extensively rewritten because:

1) The discussion on cooling rates is not clear, the concept of cooling rate has limited validity and the definition of opening and closure temperatures are not correct when used in relation to petrological studies;

We agree that, in the previous version of the paper, our use of cooling rate concept was misleading regarding the “opening and closure” temperature terminology. You will find in the following more detailed answers to this point that was also developed later in the review. Following your advice, we have extensively rewritten section 5 to focus it on the description of the numerical model results. Fig. 5 has been completed, adding thermal histories of gabbros at specified levels and their instantaneous cooling rates according to the melt accretion geometry. To avoid confusion with petrological models, we no longer use the terms “opening and closure temperatures” but we still keep Eq. 15 to define an average cooling rate useful to portray the differences of cooling versus depths for the various accretion modes. We used “high and low” temperature intervals to name these bounding values and emphasize that these average cooling rate temperature intervals are arbitrary. Fig. 6 is now clearly joined to the section 5, devoted to the description of the numerical results and clearly separated from section 6 where the petrological results are discussed.

2) Most importantly this section does not clearly show new results or conclusions, at least not in the format that is currently presented. I would strongly suggest omitting the discussion of petrological cooling models and just present the results of the thermo mechanical model. In particular it would be fantastic to see an x-y plot of T versus time of selected portions of the model, i.e. by following the position of selected tracers at different depths and horizontal displacements. In this way the authors will show the -true-cooling evolution in time and space. This by itself would be a great achievement. Petrologists will decide how their approach to thermal cooling fit into the more general thermal evolution presented here (in an x-y plotting format). In addition, it would be interesting to see how the model from this study would compare with geophysical observations as surface heat flux or topography which are directly affected by the thermal evolution of the upper and lower crust.

Following your suggestions we have redrawn Fig. 5 to describe the thermal history of cooling gabbros adding two panels for each of the G, M and S crustal accretion modes. Figs. 3 and 4 have also been redrawn. They present x-y plots of the eulerian representation of temperature for the steady state reached at the end of the runs. The new Fig. 5 depicts lagrangian representations of the thermal evolutions of tracers that are drift away by the flows. In that sense, this figure answers to your request of a x-y plot of T versus time to show the -true-cooling evolution in time and space. We have

improved its readability by adding curves of these thermal evolutions at different depth versus time. We also have added more direct information about the thermal evolution of particular trajectories at sampled depth and the values of the instantaneous cooling rate that are obtained.

Detailed comments

Page 2430: line 12-14, I am not aware of any analogy between the cooling rate defined as ICR and SCR and the cooling rate defined by experimental petrology. What does it mean "cooling rates sampled near/far from the ridge"?

To avoid confusion we no longer use these terms in the revised manuscript. Cooling rates from petrographic and/or mineral compositional data in samples of the plutonic oceanic crust are integrated cooling rates over T-t interval, which values are intrinsic to the methodologies used to derive the cooling rates. Proxies of magmatic cooling rates derived from the CSD of plagioclase in plutonic rocks (Marsh, 1988; Marsh, 1998) record the cooling of the sample in the T-t interval between the liquidus and the solidus temperature (i.e., the crystallization time). On the other hand, cooling rates based on elemental diffusion in minerals from the plutonic crust, as those based on geospeedometry, record the cooling rate in the T-t interval when exchange diffusion is effective, which depends, among other variables, on the characteristic diffusion temperature of the geospeedometer (i.e., effective diffusion and closure temperature). As most of the geospeedometric formulations these temperatures are below the basaltic solidus, we had used the denomination of "Subsolidus Cooling Rates or SCR" while the first are referred as «Igneous Cooling Rate or ICR». However, as explained above, we have reorganized the sections 5 and 6 of the paper to clarify and emphasize the differences between the petrological results and our numerical results.

Figure 5 shows, the Time-temperature (T-t) trajectories versus the emplacement depth of the plutonic crust at 20 km off-axis. T-t histories of tracers are computed along their flow. However, according to the particular configuration of the tracer trajectories, temperature will not be the same versus time and x-y coordinates during the tracer journeys. This is true for the numerical model but should also be true for gabbros in nature. Then, reaching their final emplacements in the cooled crust, gabbro cooling rates will have received different thermal histories and will be different. This is particularly true if we considered that the final cooling rate represents necessarily an integration of this history. In the new version of the paper we have brought new explanations about the locations where the average cooling rates are sensitive according to their high and low temperature intervals. The locations of the concerned isotherms have also been added in Figs. 3 and 4 to illustrate the areas of the numerical solutions that are recorded by the average cooling rates. The oceanic crust is usually sampled in crustal sections far from the ridge axis, where gabbros record protracted thermal histories since their near-liquidus temperature at their intrusion until temperatures at their final depth of emplacement off-axis.

Page 2431: line 29, Theissen-Krah et al (2011) adopted an upper cracking temperature limit of 600C. The 400-1000C temperature range covers the range of values used by several authors; some of them are cited correctly in the next few lines.

This point is an illustration both of the diversity of opinions that are often applied to particular (but potentially important regarding their consequences on the solutions) geophysical values. Scientist still debate about the bounding limits of the temperature interval over which they observe the effect

of hydrothermal cooling but, also debate about the value of the cracking temperature. This is why we have presented two series of cases illustrating possibilities of the code. With the numerical code, it is clear that it is possible to test the sensitivity of these hypotheses in terms of thermal and dynamic properties of the mid-ocean ridges and, hopefully, get clues on the cooling rates that are induced by the thermal structure of the corresponding solutions.

page 2435: line 15-16, I don't see any physical reason that justify the assumption that $\Psi_c = 2 V_p H$ and $\Psi_{lb} = 0.5 \Psi_c = V_p H$.

This result is a direct consequence of the global mass conservation that prescribes the balance between the quantity of matter flowing through the right and left sides of the computation box with the quantity of matter which enters the box from the mantle at the mid-ocean ridge. From its mathematical origin (velocity being a zero divergence field), the stream function is defined to an arbitrary constant. The value of this constant has no influence on the computation since only the stream-function differences (or derivatives) have physical senses. It seems then convenient to set this arbitrary constant in such a way that $\Psi_{lb} = 0.5 \Psi_c$ that leads to a zero stream function value at the surface. A few sentences have been added in the paper to better explain this point.

Page 2436: line 22-23, it is not clear to me why the thermal behavior of the sheeted dyke layer is simulated by instantaneous freezing.

The heat that is brought through melt injection is implicitly taken into account by the thermal boundary conditions at the ridge axis which is equal to the injection temperature from the MTZ level to the upper lens level and to the half-space cooling model conditions in the sheeted dyke layer from the upper lens to the surface. However, in this layer, the full energy equation is solved in thermal connection with the lower part of the crust (below the sheeted dyke layer). Then, the lateral propagation of heat is taken into account through the complete temperature equation, from the ridge axis to the lateral boundaries through; the conductive process, the latent heat release and the horizontal advection that occurs in the sheeted dyke layer. The vertical advection of heat is automatically cancelled by the zero vertical velocity condition in the sheeted dyke layer. However, the word freezing, employed in the first version of the paper, was misleading and has been replaced by solidification to describe modeling of the sheeted dyke layer. The Root zone of the sheeted dike complex in the Oman ophiolite goes through very abrupt cooling conditions (Nicolas et al, 2008). This layer is transitional between the magmatic system of the melt lens, convecting at 1200 °C, and a high-temperature (<1100 °C) hydrothermal system, convecting within the root zone. The whole root zone is a domain of very sharp average thermal gradient (7 °C/m) Furthermore, in nature, the injection of the sheeted dykes occurs on a very short time compared to the slow spreading process that affect the whole crust. However, it is clear that an instantaneous freezing is not an instantaneous cooling that remains, as it is shown by the thermal evolutions of the sheeted dyke layer in Figures 3 and 4, based on hydrothermal thermal exchanges with the surface and conductive heat intrusion from the lower crust. The implementation of the sheeted dyke layer has induced deep and significant changes in the functioning of the numerical code that explain it cannot be compared with the previous one published a few years ago (Machetel and Garrido, 2009).

Page 2437: line 23-25, Can I see some references from literature that support the temperature and the temperature interval for crustal melt used here (1230C, dt= 60C). The experimental petrology studies that I am aware of (Green and Ringwood, 1967, Yasuda and Fujii, 1994), show something different at -1 kbar, T solidus -1100C, T liquidus -1350C.

The values used in our study for crystallization (1230 °C, dt = 60° C) are based on the Kelemen and Aharonov (1998) (fig. 1) in their review paper Periodic Formation of Magma Fractures and Generation of Layered Gabbros in the Lower Crust beneath Oceanic Spreading Ridges. The reference has been emphasized in the text of the new version of the paper.

Page 2438: line 23-25, Viscosity of the crust (hot and cold) is extremely low, between 2-4 order of magnitude lower than commonly assumed (list of references is very long. Could the authors explain why they have chosen those values and what are the consequences of such assumption on the thermal and dynamic results?

Structural studies conducted in the Oman ophiolite indicate that the gabbro unit located between the diabase sheeted dike complex and the Moho is composed of magmatically deformed and not plastically deformed gabbros, except in the horizon just above the Moho transition where some plastic strain is locally registered [Nicolas, 1992]. This demonstrates that below the melt lens a magmatic domain extends down to the Moho and that this domain is magmatically deforming. These studies allow us to conclude that in spite of its much limited melt fraction (5-15%), the LVZ is not a solid domain deforming by plastic flow but a magmatic domain defined by its ability to deform by suspension flow [Nicolas et al., 1993; Nicolas and Ildefonse, 1996].

Page 2438 : line 24, I believe low cracking temperature is 400C (Nicolas et al, 2003) therefore the temperature of 700C adopted by the authors cannot be really considered a low T.

We agree with your remark. It is perfectly true that, according to Theissen-Kraf (2011) or Nicolas et al, (2003), 700C is rather an intermediate cracking temperature than a low one. Changes have been done in the text, figure captions, tables and figures to correct this mistake.

Page 2439: line 20, It is very difficult to see from Fig.3 any temperature variations among the 3 models (G, M, S). Wouldn't be better instead to plot the temperature difference with respect to one model, say panel a) T(G), panel b) T(G)-T(M), panel c) T(G)-T(S).

Page 2440: line 16, Fig. 4 has the same problem of Fig. 3. Plotting the temperature differences may help to visualize better the T variations of the 3 models. Is there any reason why despite a different dynamic evolution, the 3 models show very similar temperature fields?

We fully agree with your remark and decided to refer the temperature evolution in function of the accretion geometry to the temperature pattern of the Gabbro Glacier "G" solution in the new version of the paper. Figures 3 and 4 have therefore been redrawn to take these modifications into account. The text and the corresponding figure captions have also been changed.

Page 2441: line 1 and following. Fig. 5 is not clear at all. Does the plot refer to tracers along the ridge axis (x=0)?, what is the lateral position of the tracers that are plotted in the figure? It would be terrific to see a x-y plot of temperature versus time for selected tracers located at different depths and horizontal positions at time zero.

The reviewer's comment show that we failed to provide a sufficiently detailed explanation of what is represented in the Figure 5 (left column). Indeed, the horizontal coordinate of Figure 5 (left column) does not represent a distance "x", but time, whereas the vertical coordinate represents the "final" depth of emplacement of gabbro in the crust of tracers that have been injected at the ridge axis. During its journey from the ridge axis to its final emplacement (i.e., final time) in the cooled lower crust far from the ridge axis, tracers do not stay at a constant depth. This is particularly true in the case of Gabbro Glaciers "G" accretion model where the melt injected at the shallow melt lens builds the entire lower crust. This obviously induces downward trajectories near the ridge axis that are followed by the tracers. However all the tracers do not sink; some of them follow a nearly horizontal motion until their final emplacement depth in the crust. During accretion of the oceanic crust, the tracers follow the streamlines represented in Figures 3 and 4. Similarly, in the case of a Mixed shallow and transition zone lenses ("M") structures, the tracers follow down and upstream trajectories that are deciphered by the stream-function. The vertical coordinate of Figure 5 only refers to the final emplacement (final time) of the tracers in the cooled crustal section at the lateral boundaries of the model. That means that looking at the evolution of the temperature field with time in Figure 5 (left column) one can see the evolution of temperature with time of a gabbro that is now emplaced at given final depth and that have travelled along a given stream function and, therefore, the time evolution along each tracer trajectory. In fact, Figure 5 (left column) mostly shows what the reviewer wanted us to show, but having 4-variables (T-t-x-y) the x-y variable is condensed and shown at its final depth (i.e., final time) of emplacement, instead of at its initial time. A better description of this figure has been rewritten in the text and figure captions in order to facilitate the reading of such temperature evolution.

page 2441: line 20-21, The concept of opening and closing temperature in this context does not make any sense. The model presented in this study provided much more. It is possible to evaluate the instantaneous cooling rate by simply taking dT/dt at each location over time. If the authors want to make a comparison with petrological cooling models, I would suggest two possibilities: 1) compute the diffusion profiles given in the T-t path retrieved by the thermo-mechanical simulation. The computed profile should match the measured chemical profiles in real mid-ocean rocks. 2) Cooling rates based on chemical kinetics are related to the closure temperature of the geochemical system. Comparison should be done by choosing a particular system (say Ca diffusion in olivine), calculate the closure temperature and the cooling rate and then compare it with the cooling rate at the corresponding temperature from the geodynamic model.

We agree with the Reviewer that our numerical models provides much more detail of the cooling rate history of the oceanic crust through the instantaneous cooling rates; petrologically derived cooling rates are obtained from inversion of crystallization kinetic texture or mineral chemical diffusion profiles obtained in natural oceanic gabbro. In order to avoid confusion, we no longer use in the revised manuscript the term closure or open temperature, which are parameters related to the retrieval of cooling rates from chemical diffusion modeling of compositional profiles in minerals. Instead —as suggested by the Reviewer—we now provide in the revised Figure 5 (right panel) the instantaneous cooling rates along the T-t path of tracers as a function of the time and their final depth of emplacement 20 km off-axis (i.e. final time). These instantaneous cooling rates are the numerical derivatives of the T-t history of the tracers that is shown in the mid panel of Figure 5. These two new panels in Figure 5 show that:

- Instantaneous cooling rates vary along the T-t flow path. As longer time indicates longer distance from their on-axis intrusion, they also show that instantaneous cooling rates vary as a function of the distance from the ridge axis.
- Cooling rates at super-solidus conditions ($T > 1050$ C) are generally slower than those at subsolidus conditions: it is hence likely that natural proxies of cooling rate at super-solidus conditions (i.e., igneous crystal size) provides different values as those using proxies based on subsolidus intracrystalline diffusion.

It is not our intention to make a strict comparison of numerically derived cooling rates with those derived from petrological observations. As pointed out by the reviewer, this comparison would require simulation of crystallization and chemical diffusion along the cooling T-t trajectory employing numerical models of net-transfer and exchange reactions in combination with estimates of intracrystalline diffusion; the large number of variables that can be adjusted in these forward models precludes arguing for the uniqueness of any successful simulation. Such simulation is beyond the scope of our numerical model, which, however, lays the foundation for investigate forward crystallization and chemical diffusion modeling using the T-t path history (Fig.5) of each tracer obtained independently from thermo-mechanical modeling.

Page 2441: eq. 15, The definition of cooling rate given in Eq. 15 is only true for linear cooling otherwise it is useless. If the intent is a comparison with petrological models I would suggest the author to review the definition of closure temperature (Dodson, 1973), it is not an arbitrary concept (temperature at the characteristic time when D decreases by a factor equal to $e^2/3$). Furthermore, cooling rates from petrological models are dependent on the closure temperature and the geochemical system therefore a comparison of cooling rates from this study and petrological studies would require the same critical approach.

To avoid confusion with petrological models, we no longer use the terms opening and closure temperature. As discussed in the previous reply, and pointed out by the reviewer, we agree that a strict comparison with petrological cooling rates would require diffusion modeling along tracers T-t history. As one can see in Figure 5 (panel in the mid and right columns), the T-t path of tracers is nonlinear and hence the cooling rates are not constant during the accretion of the oceanic crust. We still think that Eq.15 is useful to portray relative differences of average cooling rate (Fig. 6) at arbitrary high and low ΔT temperature intervals; these arbitrary high and low temperature ΔT portray the strong variations of average cooling rate at high and low T intervals that can clearly be seen by the slope variations of curves in the new panels in the mid and right columns of Fig. 5. The actual values of average cooling rate will depend upon the choice of ΔT , but the point of Figure 6 is to show that relative variation of average cooling rate systematically vary depending on the crustal accretion mode.

Page 2445: line 5 and following, I will omit completely this part. It is not clear to me why it is so important to compare the cooling rates from this study with those retrieved from petrological studies. Beside adding a few x-y plots of T versus time, the impact of this would dramatically increase if the results would be compared with mid-ocean ridges observable data rather than numerical results using other methods. For instance, assuming that Fig. 6 does not plot cooling rates computed from Eq. 15 but the true instantaneous cooling rate versus height, it would be interesting to see a

discussion on how these extremely low cooling rates affects heat flux on the surface. Mid-ocean ridge topography could be easily computed and compared with available data.

As explained above, we have fully reorganized this part of the paper that has induced a significant reduction of the petrological cooling rate discussion. All the numerical results are now presented in section 5 and new panels in Fig. 5 (mid and right column), while we maintain a shorter discussion of petrological cooling rates in section 6.

1 Numerical model of crustal accretion and cooling rates of 2 fast-spreading mid-ocean ridges

3

4 **P. Machetel and C.J. Garrido**

5 [1]{Géosciences Montpellier, UMR5243, CNRS-UM2, cc49, 34095 Montpellier cedex 05,
6 France}

7 [2]{Instituto Andaluz de Ciencias de la Tierra (CSIC), Avenida de la Palmeras 4 Armilla, 18100,
8 Granada, Spain}

9 Correspondence to: P. Machetel (philippe.machetel@laposte.net)

10

11 **Abstract**

12 We designed a thermo-mechanical model for fast spreading mid-ocean ridge with variable
13 viscosity, hydrothermal cooling, latent heat release, sheeted dyke layer, and variable melt
14 intrusion possibilities. The model allows to take into account several accretion possibilities as:
15 the “gabbro glacier” (G), the “sheeted sills” (S) or the “mixed shallow and MTZ lenses” (M).
16 These three accretion mode have been explored assuming viscosity contrasts of 2 to 3 orders of
17 magnitude between the strong and weak phases. However they also have been explored with
18 various hydrothermal cooling conditions depending on various cracking temperatures. The mass
19 conservation, momentum equation and temperature equation have been solved using implicit and
20 half implicit, 2-D finite-difference scheme in a vorticity-stream-function framework. In a first
21 step, an eulerian approach has been used iteratively solving motion and temperature until
22 reaching steady-state solutions. The results allow assessing the effect of variable viscosity and
23 hydrothermal cooling through testing of cracking temperature of crustal rocks. In a second step,
24 lagrangian approach has been used to study the thermal histories and cooling rate of tracers
25 during their journey from the ridge axis to their final emplacement in the cooled crust. The
26 results show that instantaneous cooling rate might be used to characterize the crustal accretion
27 mode at the ridge axis. However, the results of the average cooling rate may depend significantly

28 on the choice of the chosen temperature range. The results show that numerical modeling of
29 thermo-mechanical properties of the lower crust's may bring information to characterize the
30 ridge accretion structure, hydrothermal cooling and thermal state at the fast-spreading ridges.

31 **1 Introduction**

32 There remain uncertainties in how the oceanic crust is accreted at fast mid-ocean ridges,
33 both in terms of accretion geometry but also in terms of roles and efficiencies of the cooling
34 processes like hydrothermal convective circulation. During the last decades, three main families
35 of structures have been proposed to take into account the local thermal, seismic or geophysics
36 properties of the mid-ocean ridges. Thus, Norman Sleep (1975) proposed a “gabbro glacier”
37 (henceforth “G structure”) mechanism where crystallization, occurs below the sheeted dykes at
38 the floor level of a shallow melt lens. Gabbros flow downward and outward to build the entire
39 lower oceanic crust below the sheeted dykes. This ridge structure is compatible with the
40 geophysical observations collected at the East Pacific Rise (EPR) and also with the structural
41 studies of the Oman ophiolite (Nicolas et al, 1988; Kent et al., 1990; Sinton and Detrick, 1992,
42 Henstock et al., 1993, Nicolas et al, 1993; Quick and Denlinger, 1993; Phipps Morgan and
43 Chen, 1993). However, it seems that other geophysical measurements at the EPR (Crawford
44 and Webb, 2002; Dunn et al., 2000; Nedimovic et al., 2005) and field observations from the
45 Oman ophiolite (Kelemen et al., 1997; Korenaga and Kelemen, 1997) also suggest mixed
46 accretion mechanisms (“M structures”) that involve melt lenses at both shallow depth and
47 Moho Transition Zone (MTZ) (Boudier and Nicolas, 1995; Schouten and Denham, 1995;
48 Boudier et al, 1996; Chenevez et al, 1998; Chen, 2001). Furthermore, several authors (Bédard
49 and Hebert, 1996; Kelemen et al., 1997; Korenaga and Kelemen, 1997; Kelemen and
50 Aharonov, 1998; MacLeod and Yaouancq, 2000; Garrido et al., 2001) argue in favor of melt
51 intrusions at various depths through superimposed sills at the ridge axis between the Moho and
52 the upper lens (S structure).

53 A lively scientific debate opposes these three possibilities according to their effects on
54 the thermal structure near the ridge. Indeed Chen (2001) argued against the M and S
55 propositions observing that the latent heat release during crystallization would melt the lower
56 crust if a significant quantity of gabbro were generated deep in the crust without efficient
57 extraction of heat from the hot/ductile crust by efficient hydrothermal cooling. However, the
58 scientific debate about the depth and the temperature for which hydrothermal cooling remains

59 efficient is still pending with opinions that it may be as deep as Moho, consistently with the
60 seismic observations at EPR (Dunn et al., 2000). The depth where hydrothermal convective
61 processes cool the lower crust is related to the thermal cracking temperature of gabbros that
62 depends on cooling rates, grain sizes, confining pressures and viscoelastic transition
63 temperatures (DeMartin et al, 2004). A review of this question has been proposed by Theissen-
64 Krah et al (2011), with a cracking temperature ranging from 400°C to 1000°C. Hence,
65 analyzing high temperature hydrothermal veins (900-1000°C), Bosch et al (2004) found
66 hydrous alterations of gabbro active above 975 °C, requiring hydrothermal circulations until the
67 Moho. Theirs results are in agreement with those of Koepke et al. (2005), which have proposed
68 hydrothermal activity of the deep oceanic crust at very high temperature (900-1000°C) and with
69 those of Boudier et al (2000), which proposed a temperature cracking higher than the gabbro
70 solidus. Conversely, Coogan et al (2006), bounds the hydrothermal flows in the near-axis
71 plutonic complex of Oman ophiolite at a temperature of 800°C, in agreement with the model of
72 Cherkaoui et al (2003). This very exciting scientific debate let us motivate to improve a tool
73 that may be useful exploring the effects of the melt accretion structures and hydrothermal
74 cooling hypotheses on the near ridge thermal and dynamic patterns.

75 In this work we present a series of cases calculated from a numerical code written to
76 explore the sensitivity of the thermal and dynamic patterns of the mid oceanic ridge versus the
77 hydrothermal cooling efficiency and the crustal accretion mode. However, in spite of their
78 common features, each ridge is also a particular case, with its own local properties and
79 configurations. This diversity combined with the still pending debates among the scientific
80 community about the ridge structures, the location and the strength of the hydrothermal cooling,
81 the value of the cracking temperature values, the viscosity contrast in the upper crust and the
82 feedbacks between these uncertainties requires broad parameter studies that are sometimes
83 difficult to present synthetically. Our code has been designed to allow broad, easy (and quite
84 cheap in term of computer time - from a few hours to a few days on modern PC) explorations of
85 these assumptions. This paper presents a study of the effects of the three most common melt
86 intrusion geometries, with modulation of viscosity and hydrothermal cooling according to depth
87 and cracking temperature. The Fortran sources (and data files), which are easy to customize to
88 whom may be interested, may be modified to focus on other effects as the assessments of the
89 feedback interactions between these different processes that may help to understand the

90 physical behaviors occurring at mid oceanic ridge and may help to interpret the petrologic or
91 geophysical observations.

92 We have chosen to simulate hydrothermal cooling thanks to an enhanced thermal
93 conductivity triggered by threshold cracking temperatures. In the following of Chenevez et al
94 (1998) and Machetel and Garrido (2009), the numerical approach consists to solve iteratively
95 the temperature and motion equations. They are linked by the non-linear advection terms of
96 temperature equation and by variable viscosity. In their work, Chenevez et al (1998) did not
97 open the possibility of other melt intrusion than the M structure. Later thermal models by
98 Maclennan et al. (2004 and 2005) assumed melt intrusions at several positions rather than at the
99 bottom of the ridge axis but without explicit coupling between motion and temperature. The
100 present work follows the one of Machetel and Garrido (2009) that opened the possibility of
101 modulating the melt intrusion structure with a consistent coupled solving of motion and
102 temperature equations. However, this work missed to take into account the sheeted dyke layer
103 that strongly modifies the thermal structure of the lower crust at shallow depth and was
104 inducing, in certain cases, unrealistic flow patterns at the ridge axis. This flaw is corrected in
105 the present work that also describes the physical coupling of hydrothermal effects with
106 temperature structure, crystallization, viscosity and crustal accretion mode.

107 **2 Theoretical and numerical backgrounds**

108 A global iterative process couples the temperature and motion equations in a eulerian
109 framework until reaching steady-state solutions. The latter are used, in a second step in a
110 Lagrangian approach, to compute the thermal histories of tracers along their cooling pathway in
111 the lower crust. If the global principles, the basic equations and the numerical methods described
112 by Machetel and Garrido (2009) seem similar, the new internal and boundary conditions used to
113 take into account the sheeted dyke structure induced deep modifications in the program. Thus,
114 the index of the computation grid have been subjected to several rows and columns
115 displacements in order to take into account the dyke injection and the horizontal melt injection at
116 the upper lens level. Such calculations were not possible with the code given by Machetel and
117 Garrido (2009).

118 In the present one, the 2-D computation area depends on two indexes (ranging from 1 to
119 N_x , horizontal direction; and from 1 to N_y , vertical direction). The 2-D laplacian operators for
120 motion (within a stream function – vorticity framework) and temperature are solved with finite-

121 difference alternate scheme that leads to inverse tri-diagonal matrix. Each row or column of the
122 computation grid can be split in up to five horizontal or vertical resolution segments of at least
123 three computation nodes and which extremities may potentially be used to prescribe external
124 boundary conditions (if the node is located on the external boundary of the grid) or, if the point
125 is inside the grid, internal conditions. These local properties are defined in the subroutine
126 “computation_grid” that can be carefully modified to further developments of the code if some
127 modifications as finite lengths of sills or melt lens geometries had to be taken into account.
128 Only three crustal accretion modes have been described in details in the paper: 1) the Gabbro
129 Glacier, 2) the mixed MTZ and shallow lenses, and, 3) the superimposed sill configuration.
130 They can be considered as benchmark cases to initiate numerous situations where internal
131 conditions are applied to explore the effects of injection geometries including asymmetric melt
132 intrusion at the ridge or asymmetric expansion of plates.

133 In this paper, we simulate the thermal and dynamical behaviors of the crustal parts of two
134 symmetrically diverging lithospheric plates $V_p = 50$ mm/yr, and symmetric crustal accretion.
135 Three conservative principles have been applied to ensure the momentum, mass and energy
136 conservations of the fluid including the effects of melt intrusions, latent heat releases, viscosity
137 variations and hydrothermal cooling. Within this framework the Boussinesq, mass conservation
138 equation can be written as Eq. 1.

$$139 \quad \text{div } \vec{v} = 0 \quad (1)$$

140 The mathematical properties of this zero-divergence velocity field allow introducing a stream-
141 function, ψ , from which it is possible to derive the velocity components (Eq. 2).

$$142 \quad v_x = \frac{\partial \psi}{\partial y}; v_y = -\frac{\partial \psi}{\partial x} \quad (2)$$

143 The stream-function approach ensures a mathematical checking of the zero divergence
144 condition for the velocity field. It also allows accurate, easy to operate local prescriptions of
145 discharges for melt injection. Indeed, thanks to the mathematical and physical meanings of the
146 stream-function, the difference of values between two points measures the flux of matter that

147 flows in the model through that section. Furthermore, the stream-function contour maps reveal
 148 the tracer trajectories that offer direct visualizations of the flow analogous to virtual smoke flow
 149 visualization (e.g. Von Funck et al, 2008).

150 Beyond the equation of continuity, the fluid motion must also verify the conservation of
 151 momentum through an equation that links the body forces, the pressure and the stress tensor
 152 with the physical properties of the lower crust. From the physical values given in Table one, the
 153 Prandtl number, $Pr = (c_p \eta)/k$ that characterizes the ratio of the fluid viscosity to the thermal
 154 conductivity, ranges between $2.5 \cdot 10^{15}$ and $2 \cdot 10^{18}$. Such high values allow neglecting the
 155 inertial terms of the motion equation, which finally reduces to Eq. 3,

$$156 \quad \rho \vec{g} + \nabla \cdot \underline{\tau} - \nabla p = 0 \quad (3)$$

157 where the stress tensor, τ , can be written as:

$$158 \quad \underline{\tau} = \eta (\nabla \vec{v} + \nabla \vec{v}^T). \quad (4)$$

159 Within this context, we also assume that the crustal flow remains two-dimensional in a vertical
 160 plane parallel to the spreading direction. Then, the vorticity vector $\vec{\omega} = \text{curl } \vec{v}$ reduces to only
 161 one non-zero component equivalent to a scalar value ω . After some mathematical
 162 transformations, it is possible to rewrite the continuity and momentum equations (Eqs. 1 and 3)
 163 in a system of two coupled Laplace equations for stream-function and vorticity (Eqs. 5 and 6)
 164 This formulation allows keeping all the terms that appear with the effects of a non-constant
 165 viscosity.

$$166 \quad \nabla^2 \psi + \omega = 0 \quad (5)$$

$$167 \quad \nabla^2(\eta \omega) = -4 \frac{\partial^2 \psi}{\partial x \partial y} \frac{\partial^2 \eta}{\partial x \partial y} - 2 \frac{\partial^2 \psi}{\partial x^2} \frac{\partial^2 \eta}{\partial y^2} - 2 \frac{\partial^2 \psi}{\partial y^2} \frac{\partial^2 \eta}{\partial x^2} . \quad (6)$$

168 Finally, the vorticity and stream-function equations need to be completed with an equation
 169 ensuring the conservation energy. The Left Hand Side of the temperature equation (Eq. 7)
 170 includes advection of heat through the material derivative while its Right Hand Side takes into
 171 account the hydrothermal cooling (through an enhanced thermal conductivity), the heat
 172 diffusion, the latent heat (according to the variations of the crystallization function Γ_c described
 173 later) and the heat produced by viscous heating.

$$174 \quad \rho C_p \frac{D(T)}{Dt} = \text{div } k \text{ grad } T + \rho Q_L \frac{d\Gamma_c}{dt} + \tau_{ik} \frac{\partial v_i}{\partial x_k}. \quad (7)$$

175 The non-linear advection terms of the energy equation are solved thank to half-implicit,
 176 second order accurate, alternate finite-difference schemes. Such methods are classically used
 177 for non-linear terms of partial derivative equations. This introduces constraints on time
 178 stepping, which, for temperature equation, follows the Courant criterion while it is over-relaxed
 179 for the stream-function and vorticity elliptic operators. The formalism described above offers
 180 two main advantages. The first is the numerical stability of the coupled elliptic, Laplace
 181 operators for ω and ψ . The second is the physical meaning of the stream function since its
 182 amplitude difference between two points of the grid measures the discharge ($\text{m}^3/\text{s}/\text{m}$) of matter
 183 flowing between. Furthermore, as a direct consequence of its mathematical relationship to
 184 velocity (Eq. 2), the velocity vectors are tangent to the lines of the contour map of ψ .

185 To set the geometry of the melt intrusion at the ridge axis we consider the mass conservation
 186 properties that stipulate the balance of inflows (at the bottom ridge) and outflows (through the
 187 right and left lateral boundaries) (Fig. 1). Since, in this paper, the left and right spreading rates
 188 are equal, the amplitude of the stream-function jump at the bottom of the ridge axis must be
 189 $\psi_c = 2V_p H$. The stream-function is mathematically defined to an arbitrary constant that allows
 190 setting, once in the grid, an arbitrary value. We have chosen to impose $\psi_{lb} = 0.5\psi_c$ at the
 191 bottom left boundary of the grid. Then, starting from this value, and turning all around the box,
 192 we can determine the external boundary conditions that respect the flows escaping or going in
 193 the computation box through these boundaries (Fig. 1). At the left lateral boundary the stream-
 194 function decreases linearly: ($\psi_l = \psi_{lb} - y \cdot V_p$) to reach $\psi_t = 0$ at the top. Since no fluid can
 195 escape through the upper boundary, the stream-function condition remains zero from going

196 from the left to the right upper corners. Conversely, starting from this left upper corner, the
 197 value of the stream function on the lateral right boundary decreases linearly from zero to
 198 $\psi_r = V_p(y - H)$ at depth y , and to $\psi_{lb} = -0.5\psi_c$ at the lower right corner. At the ridge, the crustal
 199 accretion mode will be set thanks to internal conditions applied to the internal values of the
 200 stream function on the two central columns of the computation grid (Fig. 1). This method does
 201 not affect the Alternate Direction Implicit (ADI) solving of the temperature and motion
 202 equations since it is easy to keep the tri-diagonal forms of the inversion matrix by splitting the
 203 horizontal or vertical resolution segments into shorter ones surrounding the location where the
 204 internal condition has to be applied. Then both ends of the segments are used by the algorithm
 205 as internal or external boundary conditions. The amplitudes of stream-function jumps, located
 206 on the two central columns of the computation grid, from the Moho to the upper lens level, now
 207 simulate the discharges of sills and lenses defining the hypothesized melt intrusion pattern
 208 (Fig. 1). Free-slip boundary conditions ($\omega = 0$) have been applied to the vorticity equation.

209 However, it is also necessary to add bottom, lateral and internal conditions to solve the
 210 temperature equation. We have considered that the oceanic crust is embedded in a half-space
 211 cooling lithosphere (Eq. 8) with a ridge temperature equal to the melt intrusion temperature
 212 $T_{Ridge} = 1280$ °C.

$$213 \quad T(x,y) = T_{Ridge} \operatorname{erf} \left(\frac{z}{2} \sqrt{\frac{\rho C_p V_p}{k_m |x|}} \right). \quad (8)$$

214 This choice of using half-space cooling thermal boundary conditions has been done to limit as
 215 possible the arbitrary prescriptions on thermal crustal surrounding while no direct
 216 measurements of temperature or dynamic states are available at MTZ. This approach follows
 217 the global geodynamic agreement that considers the half cooling law as a consistent first order
 218 approximation of temperature in oceanic lithospheres. It is also justified by the fact that, in the
 219 present study, we focus our attention on the thermal and dynamic properties near the ridge axis,
 220 far from the lateral boundaries, which effects are expected to be significantly weaker than those
 221 of accretion structures and hydrothermal cooling. Indeed, while, near the ridge, steep vertical
 222 thermal gradients ensue from hydrothermally enhanced heat extraction and motion is deeply
 223 influenced by the mass conservation and the crustal accretion mode, far from the ridge, the
 224 crustal evolution is mainly driven by thermal conduction and laminar motions. It is clear that
 225 this assumption generates side effects near the lateral boundaries of the computation area.

226 However, such situations probably exist in Nature where hydrothermal cooling induces near the
227 ridges axis enhanced vertical heat extraction that may exceed the heat transport by conductive
228 processes alone, resulting in areas cooler than the rest of the crustal part of the lithosphere.

229 The injection of the sheeted dyke layer at the ridge axis is simulated, at the roof of the
230 upper lens, by prescribing internal conditions on the stream function values. Their amplitude
231 differences correspond to the fluxes of matter required to build the left and right sheeted dyke
232 layers (Fig. 1). Above the lens, linear stream function increases are also prescribed from the
233 roof of the upper lens to the surface on the two central columns of the computation box. Then,
234 starting from these two central points and going respectively to the right and left lateral
235 boundary, the stream function is maintained constant all along the horizontal rows
236 corresponding to the sheeted dyke layer. This ensures, in the sheeted dyke layer, horizontal
237 velocities equal to the plate spreading and zero vertical velocities. Consistently with the solving
238 of temperature in the remaining of the solution, the thermal behavior in the sheeted dyke layer
239 is obtained from Eq. 7, in which the vertical advection term is cancelled by the zero value of the
240 radial velocity that ensures a conductive vertical heat transfer through the sheeted dyke layer
241 while it is conductive and advective in the horizontal direction.

242 Second-order accuracy, ADI finite-difference schemes have been applied to solve the Laplace
243 operators for stream-function, vorticity and temperature (e.g. Douglas and Rachford, 1956) with
244 a 100×600 nodes grid corresponding to a 6×40 km oceanic crust areas. The computational
245 process solves iteratively the vorticity, stream-function and temperature equations until the
246 maximum relative evolutions of the temperature between two time steps falls below 10^{-7} at each
247 node of the computational grid.

248 **3 Introducing the crust physical properties**

249 We also need to describe the links between viscosity, thermal conductivity, hydrothermal
250 cooling and temperature, continuity and motion equations. In order to minimize accuracy losses
251 that could result from numerical differentiation, the local variations of the physical parameters
252 have been written as hyperbolic, tangent-like Γ step functions (Equation 9). Such functions,
253 their derivatives and potencies are continuous and display accurate analytical expressions,
254 evolving from 0 to 1. With this formalism, 88 % of the transition occurs over a 2δ range,
255 centered on a threshold value, d_T . The quantity d may stand either for distances, temperatures or
256 crystallization. Table 1 recalls the characteristic values used for the various physical parameter

257 of this study. Most of them are subjects to still pending scientific debates. If we consider that
 258 the chosen values are representative of oceanic crust properties, we do not pretend that they are
 259 the most representative of the truth. However, they allow illustrating the sensitivity of the
 260 numerical model to the assumptions and uncertainties about the physical values and processes
 261 that affect the ocean ridge dynamics.

$$262 \quad \Gamma(d) = \frac{1}{2} \left(1 + \tanh\left(\frac{d - d_T}{\delta}\right) \right) . \quad (9)$$

263 Hence, following the work of Kelemen and Aharonov (1998) on the sharpness of the
 264 crystallization, we will consider that the melt fraction varies rapidly around a threshold
 265 temperature, $T_c = 1230^\circ\text{C}$, with a transition width $\delta T_c = 60^\circ\text{C}$ (Equation 10 and Fig.2-top). In
 266 our study, we have chosen to link the viscosity to crystallization through Eq. 11 because several
 267 authors have emphasized such steepness for the viscosity variations versus crystallization (e.g.
 268 Pinkerton and Stevenson, 1992; Marsh, 1996; Marsh, 1998; Ishibashi and Sato, 2007). In any
 269 case, the hypotheses done on the viscosity can be easily modified in the subroutine called
 270 “viscosity” of the numerical code where small changes in the description of physical
 271 dependencies of viscosity can be taken into account without changing the motion resolution
 272 scheme. The global iterative process used in our approach couples temperature, vorticity and
 273 stream function by successive solving. Therefore viscosity, which explicitly depends on
 274 temperature through Eq. 10 and 11, evolves with it all along the computing process.

275 The present work assumes that viscosity ranges between a strong, cold phase for 0% melt
 276 fraction ($\eta_s = 5 \cdot 10^{15} \text{ Pa}\cdot\text{s}$) and a weak, hot phase for 100% melt fraction ($\eta_w = 5 \cdot 10^{12} \text{ Pa}\cdot\text{s}$ or
 277 $\eta_w = 5 \cdot 10^{13} \text{ Pa}\cdot\text{s}$). This viscosity values may seem low but they belong to the range used by
 278 Chenevez et al (1998) and have been chosen in order to not smother the effects of its variations.
 279 The two curves in the lower panel of Fig. 2 displays the resulting viscosity-temperature
 280 relationship according to the contrast of viscosity assumed between the strong and weak phases.
 281 Cases involving the two viscosity contrasts, $5 \cdot 10^{12}$ versus $5 \cdot 10^{15}$ and $5 \cdot 10^{13}$ versus $5 \cdot 10^{15}$
 282 ($\text{Pa}\cdot\text{s}$) have been calculated but we will not show all the results (except later in Fig. 6) because
 283 they are so close that they are impossible to distinguish by eyes on the figures.

284
$$\Gamma_{Cryst}(x,y) = \frac{1}{2} \left(1 + \tanh \left(\frac{T(x,y) - T_{Cryst}}{\delta T_{Cryst}} \right) \right), \quad (10)$$

285
$$\eta(x,y) = \eta_w \Gamma_{Cryst}(x,y) + \eta_s (1 - \Gamma_{Cryst}(x,y))^3. \quad (11)$$

286

287 Hyperbolic, tangent-like Γ step functions have also been used to simulate hydrothermal cooling
 288 by linking the enhancement of thermal conductivity to depth and temperature. First we
 289 consider, through Equation 12, that k decreases with depth from a high value, k_H near the
 290 surface, to a low value k_L at the Moho (Numerical values are given in Table 1). Then we also
 291 assume, through Equation 13, that conductivity depends on a cracking temperature T_{crack} , for
 292 which intermediate (700 °C) and high (1000 °C) values have been tested. The resulting thermal
 293 conductivity that is used by the numerical model solving the temperature equation is obtained
 294 through Equation 14, combining Equations 12 and 13.

295
$$k_{Depth}(y) = k_L + (k_H - k_L) \frac{y}{H}, \quad (12)$$

296
$$\Gamma_{Crack}(x,y) = \frac{1}{2} \left(1 + \tanh \left(\frac{T(x,y) - T_{Crack}}{\delta T_{Crack}} \right) \right), \quad (13)$$

297
$$k(x,y) = k_L \Gamma_{Crack}(x,y) + k_{Depth} (1 - \Gamma_{Crack}(x,y)). \quad (14)$$

298 The dashed and solid lines of Figure 2 (middle panel) displays the variation of thermal
 299 conductivity obtained at the surface level ($y = H$) according to the values assumed for the
 300 cracking temperature. The two series of cases corresponding to both cracking temperature
 301 assumptions will be shown in the following.

302

303 **4 Effects of the accretion on the thermal and dynamic states of the ridge**

304

305 Three series of cases have been computed to illustrate the potential effects of the crustal
 306 accretion mode. The first is a gabbro glacier structure (called G); the second is a mixed structure
 307 with two lenses below the sheeted dyke and above the Moho (so-called M); and the third (so-
 308 called S) is a sheeted sill structure with superimposed sills delivering melt at the ridge axis. The
 309 G hypothesis consists of a melt intrusion through a shallow lens located just below the sheeted

310 dyke (4.5 km above the MTZ). The M structure assumes two shallow and deep lenses
311 respectively located just below the sheeted dyke and a few hundreds of meter above the MTZ
312 (0.3 km and 4.5 km above the MTZ). Finally, the melt delivered for the S structure comes
313 through nine sills, evenly stacked at the ridge axis, every 0.45 km, above the MTZ.

314 Fig. 3 displays the temperature patterns (color palette) and the stream functions
315 isocontours (black lines) obtained with an intermediate cracking temperature ($T_{\text{crack}} = 700^{\circ}\text{C}$) for
316 the G, M and S crustal accretion modes respectively in the top, middle and bottom panels. The
317 contours of the stream-functions reveal the trajectories resulting from the different accretion
318 scenarios. As expected, the G structure (Fig. 3, top) induces, near the ridge, predominantly
319 descending gabbro motion, while, the M motion is partly descending from the upper lens and
320 partly rising from the MTZ lens (Fig. 3, middle); and, for the S structure the numerous
321 superimposed intrusive sills induce nearly horizontal motion (Fig. 3, bottom). In all the cases, far
322 from the ridge, the stream functions converge toward laminar behaviors with cancelling of the
323 vertical velocity. The top panel of Fig. 3 also depicts the temperature field obtained for the G
324 crustal accretion mode (color scale). As they are sensitive to the heat advection and viscosity
325 through crystallization, the temperature patterns are also dependent on the crustal accretion mode
326 near the ridge. These behaviors result in variations that may locally reach several tens of degrees
327 but may remain sufficiently low to be difficult to evaluate by eyes in most of the solution. To foil
328 this inconvenience, the temperature fields obtained for the M and S structures have been
329 represented as differences with the one of the G hypothesis (two lower panels of Fig. 3). With
330 the G accretion structure context, all the melt necessary to build the entire upper crust crosses the
331 upper lens, carrying much heat at shallow level where it is efficiently extracted by the cold
332 thermal shallow gradient and enhanced hydrothermal cooling. This is no more the case for the M
333 and S crustal accretion modes. Less heat is injected at shallow lens since melt is shared with the
334 MTZ lens or with superimposed sills at the ridge axis. Compared to the thermal pattern obtained
335 for the G structure, cold anomalies appear below the upper lens where, compared to the G
336 structure temperature field, there is now a deficit of heat, and hot anomalies appear near the ridge
337 in the deeper part of the solution where more heat is now advected. Far from the ridge, the
338 influence of the melt intrusion patterns on the temperature damp rapidly to converge toward
339 conductive temperature profiles.

340 A second series of cases has been calculated with a higher gabbro cracking temperature
341 (1000°C) in order to illustrate the impact of the increase of the depth of hydrothermal cooling

342 penetration in the crust. With this higher cracking temperature, the efficiency of hydrothermal
343 cooling increases and penetrates deeper that induces colder temperatures than in the previous
344 cases (Fig. 4, top panel). However, the evolution remains small for the cases presented I this
345 study. They are more decipherable on the medium and lower panel of Fig. 4, where the lower
346 temperature are betrayed by slightly more stronger stream-function isocontours shapes,
347 characteristic of a stronger viscosity due to the slightly colder temperature. From a dynamic
348 point of view, the results, displayed on Fig. 4 remain strongly dependent on the G, M or S
349 crustal accretion modes and similar to the ones previously obtained with an intermediate
350 cracking temperature. The near-ridge gabbro motion is predominantly descending for the G
351 structure (Fig. 4, top), is partly descending and partly rising for the M structure (Fig. 4, middle);
352 and nearly horizontal for the S structure (Fig. 4, bottom).

353 As a common feature observed with both values of the cracking temperature, it appears
354 that the global temperature pattern implies steeper thermal gradient for the G accretion mode
355 than when the heat is shared with the MTZ lens or with superimposed sills at the ridge axis.
356 This result is in qualitative agreement with the observations of Chen 2001, recalled in the
357 introduction, since, in our case, at similar hydrothermal cooling, hot anomalies of
358 approximately 100 °C appears in the lower crust with the M and S crustal accretion modes
359 compared to the G accretion mode.

360 **5 Thermal history and cooling of the lower crust**

361 Figs. 3 and 4 give x-y, eulerian representation of steady state temperature patterns and
362 motions reached at the end of the computing processes. From these solutions it is possible to
363 calculate lagrangian representations of the thermal histories of tracers, following the T-t-x-y
364 (temperature, time, offset, depth) trajectories of cooling gabbros in the lower crust. The panels
365 in the left column of Fig. 5 give a representation of the thermal history of tracers during their
366 travel from the intrusion at ridge level to their final emplacement in the cooled lower crust.
367 During their transfers, the depth of tracers evolve with offset (and therefore time) according to
368 the values of the vertical velocity, which near the ridge axis is strongly dependent on the crustal
369 accretion mode. Therefor the vertical axis of Fig. 5 (left column) does not represent the depth of
370 tracers, but the final height that are reached above MTZ at the lateral boundary of the
371 computation grid. The left panels of Fig. 5 displays therefore detailed cooling histories of
372 gabbros as they could be recorded in cooled crustal sections far from the ridge axis. The panels

373 corresponding to the G and S crustal accretion modes (left column of Fig. 5) reveal monotonic
374 increases with depth of the times spent at high temperature by tracers. This is no longer the case
375 with the M crustal accretion mode, for which marked different thermal histories are obtained at
376 depths located between the melt intrusions of the upper and lower lenses. The convergence of
377 advected heat from the upper and MTZ lenses along with the slowness of the tracers near the
378 ridge increases the times spent at high temperature for the tracers crossing at that crustal level.
379 The slowness of the tracers motions are portrayed in Figs. 3 and 4 (medium panels) by the
380 smoothness of the stream-functions that denote low spatial derivatives and therefore, according
381 to Eq. 2, slow velocity components. This result explains the particular shape of the thermal
382 histories (Fig. 5, left and middle columns) for the M crustal accretion mode. Obviously, these
383 thermal and dynamic effects due to merging of sills cannot exist for the G crustal accretion
384 mode but are also present, for the S accretion structure, at the locations where the streams of
385 neighbor sills merge (Fig. 5, left bottom panel).

386 The cooling histories of tracers are also shown in the middle and right columns of Fig. 5
387 that depict the T-t evolutions and the instantaneous cooling rates of tracers for each of the G, M
388 and S melt intrusion geometries. As the depth of tracers varies during their trajectory, the
389 tracers are reported at different final depth final height that is reached above MTZ at the lateral
390 boundary of the computation grid. Hence, they portray the cooling and cooling rate evolution of
391 gabbros since their intrusion at the ridge axis until its final emplacement in cooled oceanic
392 crustal section. For the G structure, the relative positions of the thermal history curves results
393 are consistent with the monotonic evolution of thermal history described in the global thermal
394 history (ig. 5, left column, top panel). During the time evolution, the curves are regularly
395 superimposed in such an order than the curves corresponding to the closest locations near MTZ
396 at their final emplacement in the cooled crust display the hottest temperature all along the tracer
397 trajectories. This T-t evolution of tracers is rather similar for the S structure, but different to that
398 of the M structure, wherein inversions of the above curves order occur and (tracers at MTZ
399 height 1818 m, red solid line; and at 2424 m, yellow solid line) several significant times are
400 spent by tracers of shallower depth at higher temperatures than for deeper tracers (tracers at
401 MTZ height equal to 606 m, solid blue line and 1212 m, green solid line). The instantaneous
402 cooling rates (panels in the right column of Fig.5) vary along the T-t flow paths for all accretion
403 models. As longer time corresponds to farther distance from the on-axis ridge intrusion, they
404 show that, from a eulerian point of view, instantaneous cooling rates vary not only according to

405 the intrusion mode but also as a function of the distance from the ridge axis and temperature.
406 For most cases, the instantaneous cooling rates decreases with temperature and distance from
407 the ridge axis. The slowest cooling rates take place generally at temperatures above or near the
408 solidus and near the axis (i.e., shorter times). From these results, it is expected that natural
409 proxies of igneous cooling rates (e.g. crystal size; Garrido et al., 2001) will differ in extent and
410 variability from those based on intracrystalline diffusion (e.g., user different minerals and
411 diffusing species with diverse diffusion velocities. A comparison with these natural proxies of
412 cooling rate would require, however, simulation of intracrystalline diffusion and crystallization
413 along the T-t-x-y trajectories provided by our thermomechanical model.

414 To better illustrate for the variability of gabbro cooling rates along the trajectories of different
415 tracers as a function of the final distance above the MTZ, we have calculated averaged cooling
416 rates following Eq. 15 between two temperatures. In Eq. 15, dt is the time interval during which
417 temperature ranges between T_h and T_l , the high and low temperatures encountered during the
418 tracer travels.

$$419 \quad CR = \frac{(T_h - T_l)}{dt} . \quad (15)$$

420 Two arbitrary low and high temperature ranges have been chosen to illustrate these the
421 variability of cooling rates as function of temperature interval and cracking temperature. The
422 high temperature range starts at $T_h = 1275$ °C, just below our melt intrusion temperature and
423 ends with a low temperature $T_l = 1125$ °C, thus covering most of our temperature crystallisation
424 range of the lower oceanic crust. The second corresponds to an a subsolidus temperature ranges,
425 starting with $T_h = 1050$, and ending with $T_l = 850$ °C. With these temperature range choices, the
426 average cooling rates record the cooling properties in different places of the model (those for
427 which the temperature is actually ranging between the high and low boundaries). According to
428 the main locations of the 1275-1125 and 1050-850°C isotherms in Figs. 3 and 4, the first will be
429 more sensitive to the thermal structure near the ridge axis while the second will mainly record
430 the thermal structures a few kilometers off-axis.

431 The left panel of Fig. 6 presents the average cooling rate profiles obtained for the three
432 series of cases within the “crystallization” temperature range (while the right panel shows the
433 result for the “sub-solidus” temperature range). Red, green and blue curves correspond
434 respectively to the G, M and S crustal accretion modes. The results obtained with viscosity

435 contrasts of two orders of magnitude and cracking temperatures $T_{\text{crac}} = 1000 \text{ }^{\circ}\text{C}$ have been drawn
436 using heavy lines; the viscosity contrast of three orders of magnitude with cross symbols; and the
437 viscosity contrast of two orders of magnitude but $T_{\text{crac}} = 700 \text{ }^{\circ}\text{C}$ with dashed lines. The
438 comparisons of the relative location of the solid and cross shaped symbols in the various curves
439 of Fig. 6 confirm that increases of two to three orders of magnitude viscosity contrasts have
440 almost no effect on the results. In all the cases, the cross symbols superimpose almost perfectly
441 with the corresponding heavy curves. The comparisons of solid line curves with dashed lines
442 provide visualizations of the effects of the cracking temperature level. In the previous section,
443 comparing Figs. 3 to 4, we emphasized that the final effects of the cracking temperature on the
444 global thermal patterns of solutions was remaining of a few tens of degrees. Nevertheless, the
445 slight deviations of trajectories and distortions of temperature due to these changes modify the
446 average cooling rates of Fig. 6. The slightly colder environments, induced by the enhancement of
447 the deep, near ridge cooling with the high cracking temperature contexts expose the gabbro to
448 lower temperatures that results in higher cooling rates. However, these effects are weak and the
449 slopes of the average cooling rates curves with depth remain almost unchanged.

450 For the average cooling rate profiles obtained with the lower temperature range, the
451 effects of variable cracking temperature are similar but less pronounced (Fig. 6, right panel). In
452 these cases the sampled areas of the model are far from the ridge axis, where the motion
453 become laminar and the vertical temperature evolution tend toward conductive profile. It results
454 decreases of the cooling rate differences versus accretion mode and gathering of the curves
455 depicting the average cooling rates obtained for the different crustal accretion modes. The
456 differences among the G, M and S accretion models are better discriminated by the average
457 cooling rate obtained with the higher temperature range (Fig. 6, left). As result, which it might
458 been expected from instantaneous cooling rate evolution (Fig. 5), the profiles of integrated
459 cooling rates with distance from the MTZ are monotonic for the G structure (red curves),
460 display bi-modal shapes with marked minimum values at the levels where the flows from the
461 upper and lower lenses merge for the M structure, and present saw tooth-like shapes for the S
462 structures where the sills are merged. The same analysis is more difficult to apply to the
463 average cooling rate profiles obtained with lower temperature range (Fig. 6, right). Indeed, the
464 shift of the sampled areas far from the ridge and the lower value of the low temperature prevent
465 from calculating the average cooling rates in the lower part of the lower crust. It is clear from
466 these results that the ability of average cooling rate to differentiate the various accretion

467 scenarios will be better for the higher temperature ranges that actually correspond in the models
468 to locations where the temperature and motions are the most influenced by the crustal accretion
469 mode.

470 **6 Summary and discussion**

471 Our thermo-mechanical model offers a tool to explore the effects of deep, near off-axis
472 hydrothermal cooling, viscosity contrast variable and crustal accretion mode on the thermal and
473 dynamic patterns of flow near fast spreading mid ocean ridges. The series of cases presented in
474 this paper simulate gabbro glacier “G”, mixed MTZ and shallow lenses “M” or superimposed
475 sills “S” crustal accretion modes, with various viscosity contrasts and, through the effects of a
476 cracking temperature, various depths of hydrothermal cooling. Other accretion modes may be
477 explored with our thermo-mechanical model, however. The differences of thermal structures
478 obtained for the G, M and S hypotheses induce minor differences in temperature with depth and
479 distance off-axis, which make it difficult to use temperature (or geophysical proxies of
480 temperature) to discriminate among different crustal accretion scenarios. All cases investigated
481 in this paper are consistent with the temperature structure at the ridge axis derived from
482 geophysical studies at the East Pacific Rise (Dunn et al. 2000; Singh et al. 2006) that show a 8-
483 12 km wide magma chamber ($T < 1150^{\circ}\text{C}$) with steep isotherms near the ridge axis. However,
484 our results indicate that combinations of near-ridge flow patterns with local temperature
485 differences both depending on the crustal accretion mode induce significant differences in the
486 cooling histories of lower crustal gabbros. These differences are portrayed variations of the
487 instantaneous cooling rates with time (Fig.5) and average cooling rate with distance from the
488 MTZ (Fig. 6) of the lower crust, which can both be useful to discriminate among different
489 crustal accretion scenarios. Depending on the temperature interval used to average the
490 instantaneous cooling rate, the profiles of the cooling rate with distance from the MTZ are
491 however more or less able to discriminate among different crustal accretion modes. Cooling
492 rates obtained from averaging a higher temperature interval sample areas of the mode that are
493 closer to the ridge axis, where the differences of average cooling rates are more discriminant of
494 the crustal accretion mode. Conversely, average cooling rates obtained with a lower
495 temperature interval sample areas of the accretion models where the thermal state and dynamic
496 of the lower crust converge, respectively, toward a vertical conductive temperature profile and
497 laminar motions. Hence, they are less discriminant of the accretion model.

498 Cooling rates obtained from petrographic and/or mineral compositional data in crustal samples
499 ophiolite or active mid-ocean ridges are integrated of cooling rates over T-t interval, which
500 values are intrinsic to the methodologies used to derive the cooling rates. Absolute quantitative
501 cooling rates of the plutonic crust have been determined by thermochronology (John et al.,
502 2004), Crystal Size Distribution (CSD) of plagioclase in plutonic rocks (Marsh, 1988; Marsh,
503 1998, Garrido et al, 2001), an elemental diffusion in minerals from the plutonic crust based on
504 geospeedometry (Coogan et al., 2002; Coogan et al., 2007; VanTongeren et al., 2008). These
505 different proxies of magmatic cooling rates record the cooling of oceanic gabbros in T-t interval
506 between the liquidus and the solidus temperature (i.e., the crystallization time; CSD of Garrido
507 et al., 2001) or elemental diffusion in minerals from the plutonic crust, as those based on
508 geospeedometry (Coogan et al., 2002; Coogan et al., 2007; VanTongeren et al., 2008), record
509 the cooling rate in the T-t interval where a characteristic exchange diffusion is effective.

510 Garrido et al. (2001) measured CSD from plagioclase in the Khafifah section of the
511 Wadi Tayin massif and found evidence of a transition from conduction dominated cooling in
512 the lower gabbros (below 1500 m above Moho) to hydrothermally dominated cooling in the
513 upper gabbros (above 2500 m). They concluded theirs data were consistent with the S model of
514 accretion. However, theirs cooling profiles did not show the same kind of evolution with depth
515 than the average cooling rate presented in this numerical study. They were displaying upper
516 crust value 1.5 to 2 times faster than lower crust values. To the light of the present numerical
517 results, this could be compatible with the three accretion structure hypotheses. Coogan et al.
518 (2002), using the Ca diffusion in olivine from Wadi Abyad massif crustal section reported that
519 cooling rates decrease rapidly with depth by several orders of magnitude between the top and
520 bottom of the lower crust. They also mention that the cooling depth profile matches that of
521 conductive models. These authors concluded in favor of a crystallization occurring inside of the
522 magmatic chamber and hence a G ridge structure. VanTongeren et al. (2008) extended the work
523 of Coogan et al. (2002) in the Wadi Tayin massif of the Oman ophiolite. The two studies differ
524 both in amplitudes and shapes of cooling rates profiles (see the comparison in Figure 7 of
525 VanTongeren et al. (2008) and Figure 3 of MacLennan et al (2005)). VanTongeren et al. (2008)
526 argued that these differences reflect distinct thermal histories due to differences in crustal
527 thickness and/or the geodynamic setting. However, the cooling rates recalculated by
528 VanTongeren et al. (2008) using Coogan's data (Coogan et al., 2002) remain several orders of
529 magnitude faster than the ones calculated by the former. Such differences between the results of

530 VanTongeren (2008) and those of Cogan et al (2002) suggest, as recalled by Coogan et al
531 (2002) and MacLennan et al (2005), that large uncertainties in petrological may probably come
532 from a deficit of constraints on the values of diffusion parameters.

533 The present thermomechanical model provides much more detail of cooling rate history
534 of the oceanic crust through the instantaneous cooling rates than that obtained from natural
535 proxies. A strict comparison with petrological derived cooling rates would require simulation of
536 crystallization and chemical diffusion along the T-t-x-y trajectories employing numerical
537 models of net-transfer and exchange reactions in combination with estimates of intracrystalline
538 diffusion. Such simulation is beyond the scope of the numerical model, which, however, lays
539 the foundation for this development. The results of our model indicate, however, that some
540 assumptions often made using petrological derived cooling rates to discriminate between
541 accretion models are simplistic. For instance, our results shows that cooling rates at super-
542 solidus conditions are generally slower than those subsolidus conditions. It is hence likely that
543 natural proxies of cooling rate at super solidus conditions will provide different values as those
544 using proxies based on subsolidus intracrystalline diffusion. The present models shows that
545 monotonic variations of the cooling rates with depth are not necessarily symptomatic of
546 conductive cooling or a G crustal accretion structure (Coogan et al. 2002), as this variation may
547 be also produced by a S accretion geometry.

548 In spite and because of these uncertainties, our results suggest that numerical modeling of
549 crustal accretion modes and their consequences in terms of instantaneous and average cooling
550 rates may provide efficient tools to try to discriminate between different crustal accretion
551 modes at fast spreading mid-ocean ridges. Further use of the present thermomechanical model to
552 discriminate between crustal models would require benchmarking the results with geophysical
553 observables.

554

555 **Acknowledgments**

556 We thank Jill VanTongeren for kindly sharing data on cooling rates from the Oman ophiolite.
557 Lawrence Coogan, John McLennan and Tim Henstock whose critics helped us to improve the
558 numerical model and the two anonymous referees, which comments have greatly, contribute to
559 improve the manuscript.

560

561

562

563 **References**

- 564 Bédard, J.H. and Hebert, R., The lower crust of the Bay of Islands ophiolite, Canada
565 Petrology, mineralogy, and the importance of syntexis in magmatic differentiation
566 in ophiolites and at ocean ridges. *J. Geophys. Res.-Solid Earth*, 101(B11): 25105-
567 25124, 1996.
- 568
569 Bosch, D., Jamais, M., Boudier, F., Nicolas, A., Dautria, J.M., Agrinier, P., Deep and
570 high-temperature hydrothermal circulation in the Oman ophiolite - Petrological and
571 isotopic evidence. *Journal of Petrology*, 45(6): 1181-1208, 2004.
- 572
573 Boudier, F. and Nicolas, A., Nature of the Moho transition zone in the Oman
574 Ophiolite. *Journal of Petrology*, 36(3): 777-796, 1995.
- 575
576 Boudier, F. Godard, M., Armbruster, C., Significance of noritic gabbros in the gabbro
577 section of the Oman ophiolite, *Marine Geophys. Res.*, 21, 307-326, 2000.
- 578
579 Boudier, F., Nicolas, A., Ildefonse, B., Magma chambers in the Oman ophiolite: fed
580 from the top and the bottom, *Earth Planet. Sci. Lett.*, 144, 239-250, 1996.
- 581
582 Chen, Y.J., Thermal effects of gabbro accretion from a deeper second melt lens at the
583 fast spreading East Pacific Rise. *Journal of Geophysical Research-Solid Earth*,
584 106(B5): 8581-8588, 2001.
- 585
586 Chenevez, J., Machel, P. and Nicolas, A., Numerical models of magma chambers in
587 the Oman ophiolite. *Journal of Geophysical Research-Solid Earth*, 103(B7): 15443-
588 15455, 1998.
- 589
590 Cherkaoui, A.S.M., Wilcock, W.S.D., Dunn, A.R. and Toomey, D.R., A numerical
591 models of hydrothermal cooling and crustal accretion at a fast spreading mid-ocean
592 ridge, *Geochem. Geophys. Geosys.*, 4, 9, 8616, doi: 10.1029/2001GC000215, 2003.
- 593
594 Coogan, L.A., Hain, A., Stahl, S. and Chakraborty, S., Experimental determination of
595 the diffusion coefficient for calcium in olivine between 900 degrees C and 1500
596 degrees C. *Geochimica Et Cosmochimica Acta*, 69(14): 3683-3694, 2005.
- 597
598 Coogan, L.A., Jenkin, G.R.T. and Wilson, R.N., Constraining the cooling rate of the
599 lower oceanic crust: a new approach applied to the Oman ophiolite. *Earth and
600 Planetary Science Letters*, 199(1-2): 127-146, 2002.
- 601
602 Coogan, L.A., Howard, K.A., Gillis, K.M., Bickle, M.J., Chapman, H., Boyce, A.J.,
603 Jenkin, G.R.T., Wilson, R.N., Chemical and thermal constraints on focused fluid
604 flow in the lower oceanic crust, *Am. J. Sciences*, 306, 389-427, DOI
605 10.2475/06.2006.01, 2006.
- 606
607 Coogan, L.A., Jenkin, G.R.T. and Wilson, R.N., Contrasting cooling rates in the lower
608 oceanic crust at fast- and slow-spreading ridges revealed by geospeedometry.
609 *Journal of Petrology*, 48(11): 2211-2231, 2007.

610
611 Crawford , W.C. and Webb, S.C., Variations in the distribution of magma in the lower
612 crust and at the Moho beneath the East Pacific Rise at 9 degrees -10 degrees N.,
613 Earth & Planet. Sci. Lett., 203: 117-130, 2002.
614
615 DeMartin, Brian, Hirth, G., Evans, B., Experimental constraints on thermal cracking of
616 peridotite at oceanic spreading centers, Mid-Ocean Ridges: Hydrothermal
617 Interactions between the lithosphere and Oceans, Geophysical Monograph Series
618 148, 167-186, 2004.
619
620 Douglas, J., Rachford, H.H., On the numerical solution of heat conduction problems in
621 two and three space variables, Trans. Am. Math. Soc., 82, 966-968, 1956.
622
623 Dunn, R.A., Toomey, D.R. and Solomon, S.C., Three-dimensional seismic structure
624 and physical properties of the crust and shallow mantle beneath the East Pacific
625 Rise at 9° 30' N. Journal of Geophysical Research-Solid Earth, 105(B10): 23537-
626 23555, 2000.
627
628 Garrido, C.J., Kelemen, P.B. and Hirth, G., Variation of cooling rate with depth in
629 lower crust formed at an oceanic spreading ridge: Plagioclase crystal size
630 distributions in gabbros from the Oman ophiolite. Geochemistry Geophysics
631 Geosystems, 2, 1041, doi:10.1029/2000GC000136, 2001.
632
633 Henstock, T.J., Woods, A.W., White, R.S., The accretion of oceanic crust by episodic
634 sill intrusion, J. Geophys. Res., 98, 4143-4161, 1993.
635
636 Ishibashi, H., Sato, H., Viscosity measurements of subliquidus magmas : Alkali olivine
637 basalts from the Higashi-Matsuura district Southwest Japan, J. Volc. Geoth. Res.,
638 160, 223-238, 2007.
639
640 John, B.E., Foster, D.A., Murphy, J.M., Cheadle, M.J., Baines, A. G., Fanning, C.M.,
641 Copeland, P., Determining the cooling history of in situ lower oceanic crust –
642 Atlantis Bank, SW Indian Ridge, Earth Planet. Sci. Lets., 222, 145-160, 2004.
643
644 Kelemen, P.B. and Aharonov, E., Periodic formation of magma fractures and
645 generation of layered gabbros in the lower crust beneath oceanic spreading ridges.
646 "W. R. Buck, T. Delaney, A. Karson and Y. Lagabriele" (Editor), In: Faulting and
647 Magmatism at Mid-Ocean Ridges, Geophysical Monograph Series, vol. 106,
648 ISBN:0-87590-089-5, 267-289, 1998.
649
650 Kelemen, P.B., Koga, K. and Shimizu, N., Geochemistry of gabbro sills in the crust
651 mantle transition zone of the Oman ophiolite: Implications for the origin of the
652 oceanic lower crust. Earth and Planetary Science Letters, 146(3-4): 475-488, 1997.
653
654 Kent, G.M., Harding, A.J. and Orcutt, J.A., Evidence for a smaller magma chamber
655 beneath the East Pacific Rise at 9°30'N. Nature, 344: 650-653, 1990.
656

- 657 Koepke, J., Feig, S.T. and Snow, J., Hydrous partial melting within the lower oceanic
658 crust. *Terra Nova*, 17(3): 286-291, 2005.
- 659
- 660 Korenaga, J. and Kelemen, P.B., Origin of gabbro sills in the Moho transition zone of
661 the Oman ophiolite: Implications for magma transport in the oceanic lower crust.
662 *Journal of Geophysical Research-Solid Earth*, 102(B12): 27729-27749, 1997.
- 663
- 664 Machetel, P. and Garrido, C.J., A thermo-mechanical model for the accretion of the
665 oceanic crust at intermediate to fast spreading oceanic ridges. *Geochemistry
666 Geophysics Geosystems*, 10: Q03008, doi:10.1029/2008GC002270, 2009.
- 667
- 668 MacLennan, J., Hulme, T. and Singh, S.C., Thermal models of oceanic crustal
669 accretion: Linking geophysical, geological and petrological observations.
670 *Geochemistry Geophysics Geosystems*, 5, Q02F25, doi:10.1029/2003GC000605,
671 2004.
- 672
- 673 MacLennan, J., Hulme, T. and Singh, S.C., Cooling of the lower oceanic crust.
674 *Geology*, 33(5): 357-360, 2005.
- 675
- 676 MacLeod, C.J. and Yaouancq, G., A fossil melt lens in the Oman ophiolite:
677 Implications for magma chamber processes at fast spreading ridges. *Earth and
678 Planetary Science Letters*, 176: 357-373, 2000.
- 679
- 680 Marsh, B., D., Crystal size distribution (CSD) in rocks and the kinetics and dynamics
681 of crystallization I. Theory. *Contrib. Mineral. Petrol.*, 99: 277-291, 1988.
- 682
- 683 Marsh, B.D., Solidification fronts and magmatic evolution, *Mineralogical Magazine*,
684 60, 5-40, 1996.
- 685
- 686 Marsh, B.D., On the interpretation of crystal size distributions in magmatic systems.
687 *Journal of Petrology*, 39: 553-599, 1998.
- 688
- 689 Nedimovic, M.R., Carbotte, S.M., Harding, A.J., Detrick, R.S., Canales, P., Diebold,
690 J.B., Kent, G.M., Tischer, M., Babcock, J.M., Frozen magma lenses below the
691 oceanic crust. *Nature*, 436(7054): 1149-1152, 2005.
- 692
- 693 Nicolas, A., Boudier, F., Ceuleneer, G., Mantle flow patterns and magma chambers at
694 ocean ridges – evidence from the Oman ophiolite, *Marine Geophysical Researches*,
695 9, n°4, 293-310, 1988.
- 696
- 697 Nicolas, A., Freydier, Cl., Godard, M., Boudier, F., Magma chambers at oceanic ridges
698 : How large?, *Geology*, 21, 53-5, 1993.
- 699
- 700 Nicolas, A., Boudier, F., Koepke, J., France, L., Ildefonse, B., Mevel, C., Root zone of
701 the sheeted dike complex in the Oman ophiolite, *Geochem. Geophys. Geos.*, 9, n° 5,
702 Q05001, doi: 10.1029/2007GC001918, 2008.

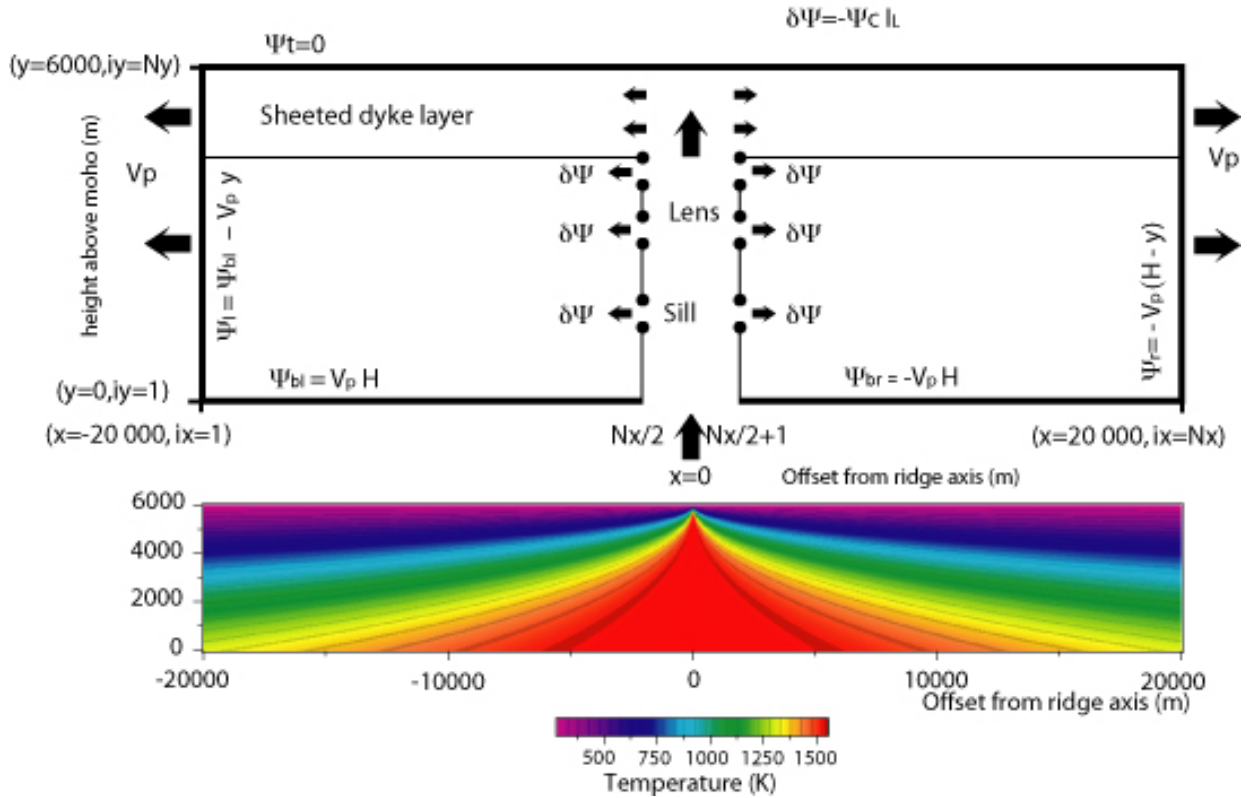
703 Phipps Morgan, J. and Chen, Y.J., The genesis of oceanic-crust. Magma Injection,
704 hydrothermal circulation, and crustal flow. *Journal of Geophysical Research-Solid*
705 *Earth*, 98(B4): 6283-6297, 1993.
706
707 Pinkerton, H., Stevenson, R.J., Methods of determining the rheological properties of
708 magmas at sub-liquidus temperatures, *J. Volc. Geoth. Res.*, 53, 47-66, 1992.
709
710 Quick, J.E., Denlinger, R.P., Ductile deformation and the origin of layered gabbro in
711 ophiolites, *J. Geophys. Res.*, 98, 14,015-14,027, 1993.
712
713 Schouten, H. and Denham, C., Virtual ocean crust, *EOS, Trans. AGU*, 76: p. S48,
714 1995.
715
716 Singh, S.C., Harding, A.J., Kent, G.M., Sinha, M.C., Combier, V., Tong, C.H., Pye,
717 J.W., Barton, P.J., Hobbs, R.W., White, R.S., Orcutt, J.A., Seismic reflection
718 images of the Moho underlying melt sills at the East Pacific Rise, *Nature*, 442, 287-
719 290, 2006.
720
721 Sinton, J.M. and Detrick, R.S., Mid-ocean ridge magma chambers. *Journal of*
722 *Geophysical Research*, 97: 197-216, 1992.
723
724 Sleep, N. H., Formation of oceanic crust: Some thermal constraints, *J. Geophys. Res.*,
725 80, 4037-4042, 1975.
726
727 Theissen-Krah, S., Lyer, K., Rüpke, L.H., Phipps Morgan, J., Coupled mechanical and
728 hydrothermal modeling of crustal accretion at intermediate to fast spreading ridges,
729 *Earth Planet. Sci. Lett.*, 311, 275-286, 2011.
730
731 VanTongeren, J.A., Kelemen, P.B. and Hanghoj, K., Cooling rates in the lower crust
732 of the Oman ophiolite: Ca in olivine, revisited. *Earth and Planetary Science Letters*,
733 267(1-2): 69-82, 2008.
734
735 Von Funck, W., Weinkauff, T., Theisel, H., Seidel, HP., Smoke surfaces: An interactive
736 flow visualization technique inspired by real-world flow experiment, *IEEE*
737 *Transactions on Visualization and Computer Graphics*, vol 14, n°6, pp. 1396-1403,
738 doi: 10.1109/TVCG.2008.163, 2008.
739

740 **Table 1**

Notations	Name (Units)	Values
Fluid velocity	v (m/s)	
Horizontal coordinate (offset from ridge)	x (m)	-L to L
Vertical coordinate (height above Moho)	y (m)	0 to H
Vertical coordinate (depth below seafloor)	z (m)	0 to H
Temperature	T ($^{\circ}\text{C}$)	
Pressure	p (N/m^2)	
Strain	τ (N/m^2)	
Stream function	ψ (m^2/s)	
Vorticity	ω (s^{-1})	
Time	t (s)	
Density	ρ (kg/m^3)	
Latent heat of crystallization	Q_L (J/kg)	$500 \cdot 10^3$
Heat capacity by unit of mass	C_p (J/kg K)	10^3
Gravity acceleration	g (m/s^2)	
Crystallization function	Γ_{Cryst} (-)	0 to 1
Thermal conductivity	k (J/(m s K))	
High thermal conductivity	k_h (J/(m s K))	20.
Low thermal conductivity	k_l (J/(m s K))	2.5
Intermediate Cracking temperature	T_{Crac} ($^{\circ}\text{K}$; $^{\circ}\text{C}$)	973 ; 700
High Cracking temperature	T_{Crac} ($^{\circ}\text{K}$; $^{\circ}\text{C}$)	1273 ; 1000
Cracking temperature interval	T_{Crac} ($^{\circ}\text{K}$; $^{\circ}\text{C}$)	60 ; 60
Dynamic viscosity	η (Pa.s)	
Weak viscosity (weak phase)	η_w (Pa.s)	$5 \cdot 10^{12}$ or $5 \cdot 10^{13}$
Strong viscosity (strong phase)	η_s (Pa.s)	$5 \cdot 10^{15}$
Mid crystallization temperature	T_{Cryst} ($^{\circ}\text{K}$; $^{\circ}\text{C}$)	1503 ; 1230
Crystallization temperature interval	δT_{Cryst} ($^{\circ}\text{K}$; $^{\circ}\text{C}$)	60 ; 60
Crust thickness from Moho to sea floor	H (m)	6000
Distance from ridge to lateral box boundary	L (m)	20 000
Right and left symmetric spreading plate velocity	V_p (m/s ; m/year)	$1.5844 \cdot 10^{-9}$; $5 \cdot 10^{-2}$
Ridge temperature for lithospheric cooling	T_{Ridge} ($^{\circ}\text{K}$; $^{\circ}\text{C}$)	1553 ; 1280
Lens height above Moho	y_l (m)	4500
Total lineic ridge discharge	ψ_c (m^2/s)	$1.9013 \cdot 10^{-5}$
Stream function left bottom boundary	ψ_{lb} (m^2/s)	$0.9506 \cdot 10^{-5}$
Stream function lateral left boundary	ψ_l (m^2/s)	
Stream function top boundary	ψ_t (m^2/s)	0
Stream function lateral right boundary	ψ_r (m^2/s)	
Stream function right bottom boundary	ψ_{rb} (m^2/s)	$-0.9506 \cdot 10^{-5}$
Seafloor temperature	T_{sea} ($^{\circ}\text{K}$; $^{\circ}\text{C}$)	273 ; 0
Melt intrusion temperature	T_{Melt} ($^{\circ}\text{K}$; $^{\circ}\text{C}$)	1553 ; 1280
High T for average cooling rate (igneous)	T_h ($^{\circ}\text{K}$; $^{\circ}\text{C}$)	1548 ; 1275
Low T for average cooling rate (igneous)	T_l ($^{\circ}\text{K}$; $^{\circ}\text{C}$)	1398 ; 1125
High T for average cooling rate (sub-solidus)	T_h ($^{\circ}\text{K}$; $^{\circ}\text{C}$)	1323 ; 1050
Low T for average cooling rate (sub-solidus)	T_l ($^{\circ}\text{K}$; $^{\circ}\text{C}$)	1123 ; 850
Number of horizontal grid points	N_x (grille1 ; grille 2)	600 ; 1798
Number of vertical grid points	N_y (grille1 ; grille 2)	100 ; 298

741

742 Table 1: Notations and values used in this paper.



743

744

745

746

747

748

749

750

751

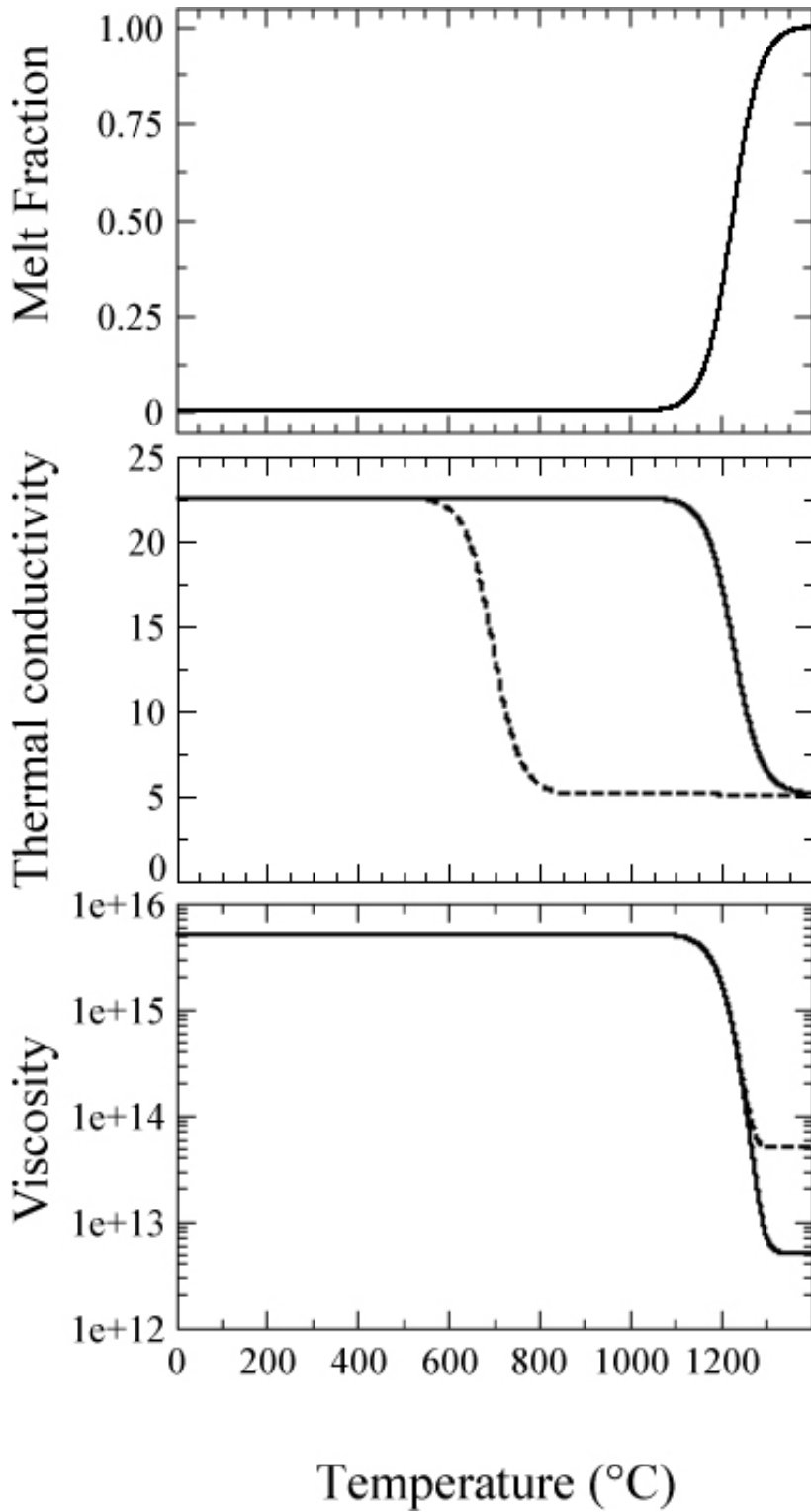
752

753

754

755

Figure 1: Sketch of the stream-function (top) and temperature (bottom) internal and boundary conditions. The computation grid is composed of N_x vertical columns (from 1 to N_x , $x = -L$ to $x = L$) and N_y rows (from 1 to N_y , $y = 0$ to $y = H$). The ridge axis is located between the points $N_x/2$ and $(N_x/2)+1$ where the amplitude of the stream-function jump is equal to $\Psi_c = 2 V_p H$, the total flux of crust that leaves the computation box through the left and right lateral boundaries. At the top of the crust and at the Moho level, Ψ is constant (impervious boundary), except at the ridge axis. Its bottom left value has been set to $\Psi_{bl} = V_p H$. Internal stream function jumps, $\delta\Psi$, on the two central columns, drive the melt intrusion through sills and/or lenses. Initial and internal boundary conditions are also applied to the temperature field according to a half-space lithospheric cooling law (Eq. 14).



756

F

757

758

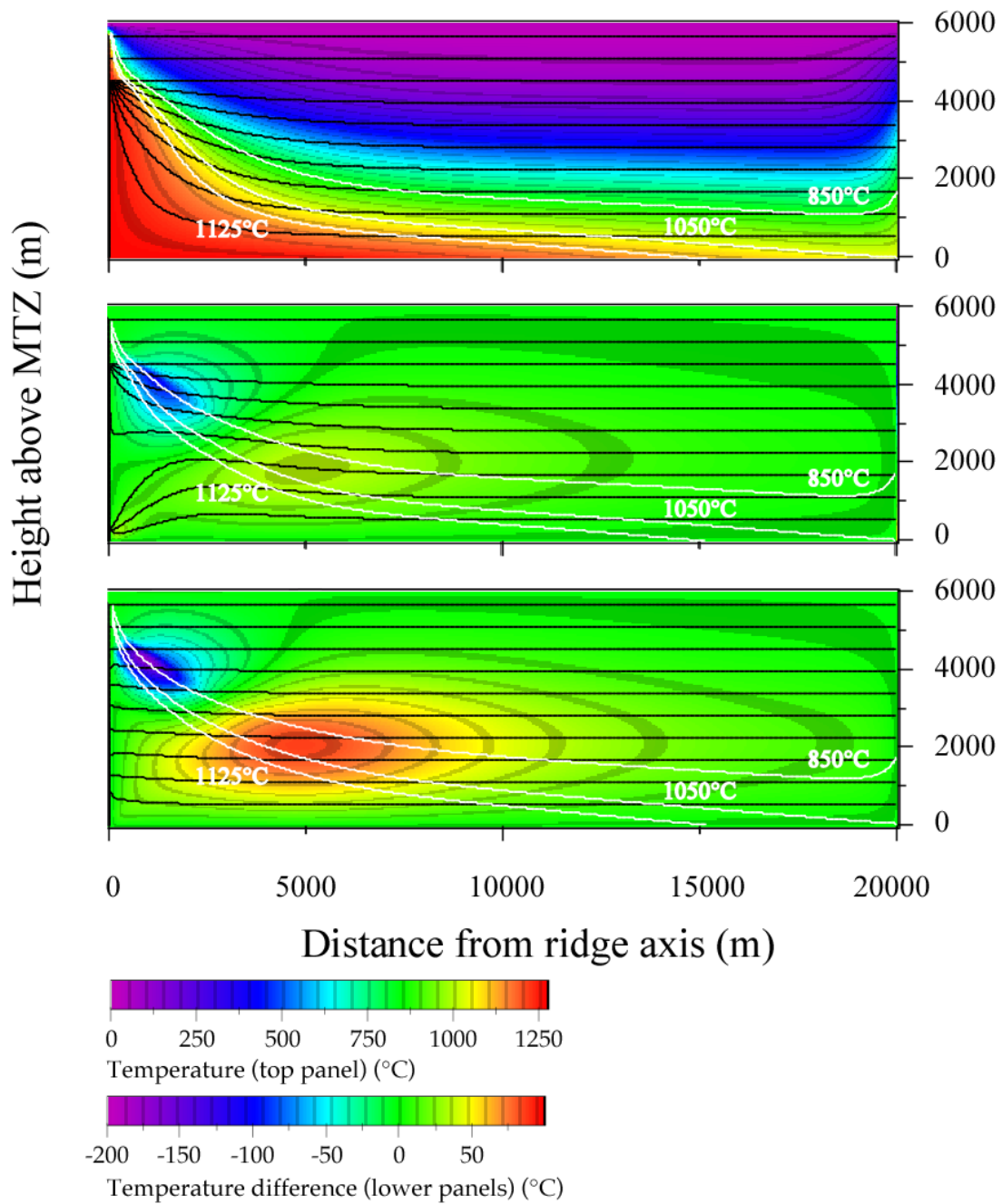
759

760

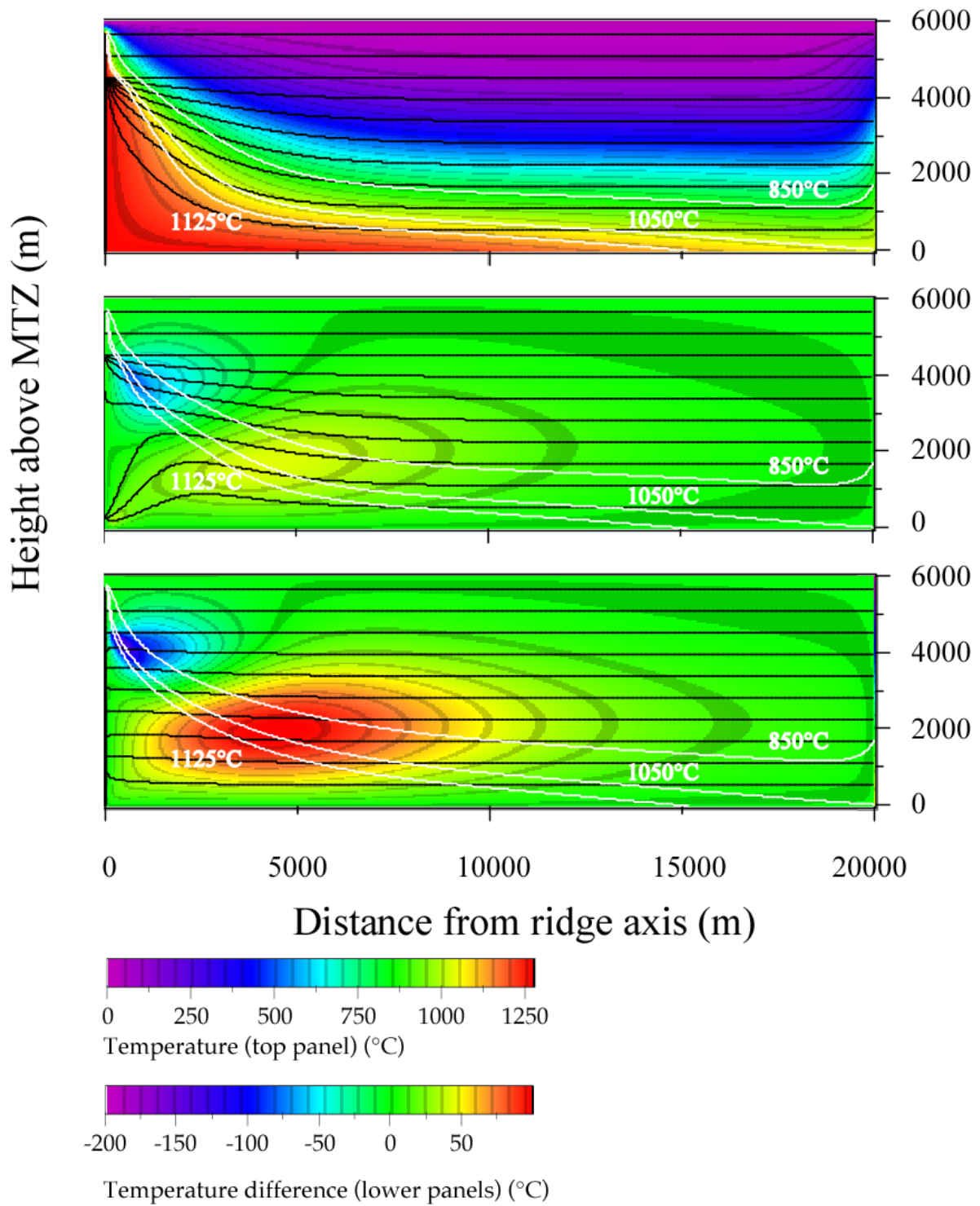
761

762

Figure 2: top: Amplitude of the melt fraction Γ_{Cryst} versus temperature; middle: thermal conductivity k at the surface of the model (dashed curve: $T_{Crac} = 700^\circ\text{C}$; solid curve: $T_{Crac} = 1000^\circ\text{C}$); bottom: dynamic viscosity η versus temperature (dashed curve: $\eta_w = 5.10^{13}$ Pa.s, solid curve: $\eta_w = 5.10^{12}$ Pa.s).



763
 764 *Figure 3: Temperature and stream function obtained for the G (top), M (middle)*
 765 *and S (bottom) crustal accretion modes. To increase the readability of the figure the*
 766 *temperature field obtained for the G structure has been represented in the top panel.*
 767 *Values of temperature correspond to the top color scale. For the M and S structures*
 768 *(medium and lower panels, the temperatures are represented as difference with the gabbro*
 769 *glacier (G) structure above. The direction of velocity is directly given by the stream-*
 770 *function contours (black lines). White lines display the locations of the 1125, 1050 and*
 771 *850°C isotherms that will be used for the computation of the average cooling rates (see*
 772 *text and Fig. 6). The results have been obtained with an intermediate hydrothermal*
 773 *cracking temperature $T_{crac} = 700^{\circ}\text{C}$ and a viscosity contrast of two orders of magnitudes.*
 774



775

776

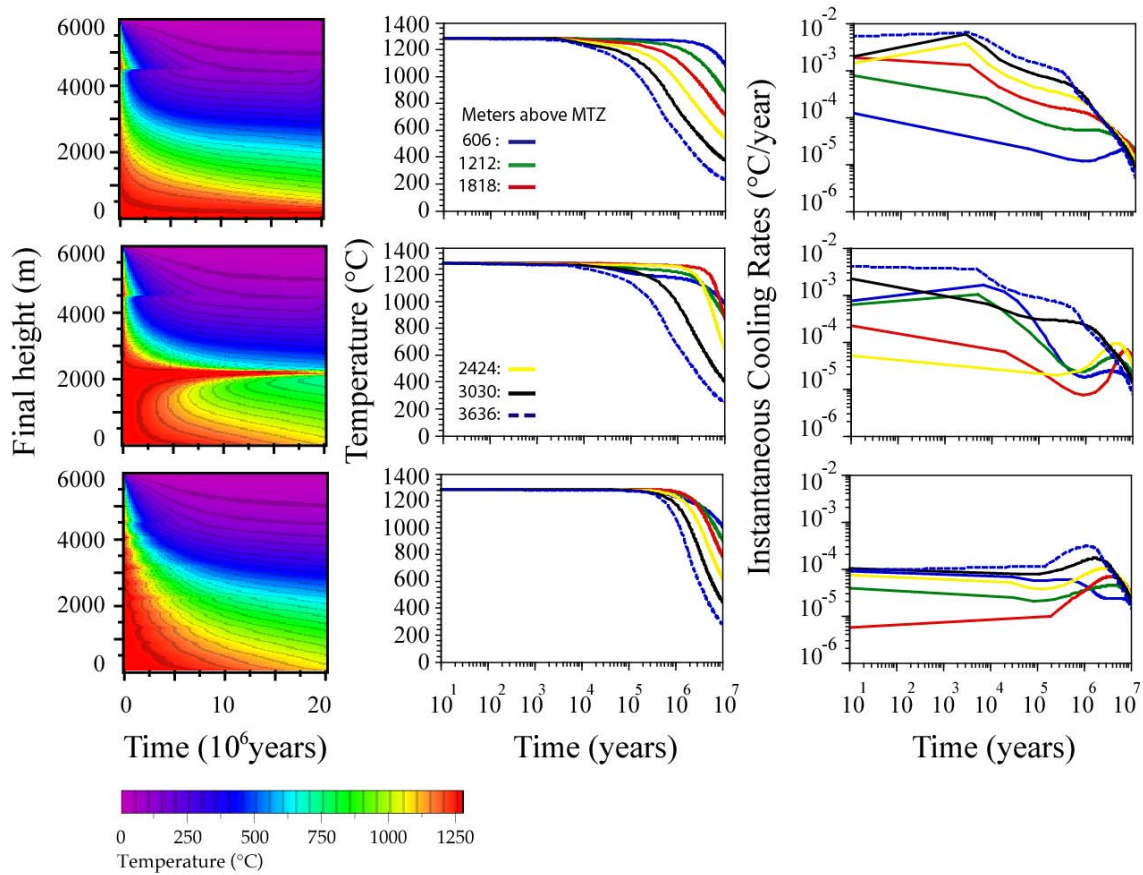
777

778

779

780

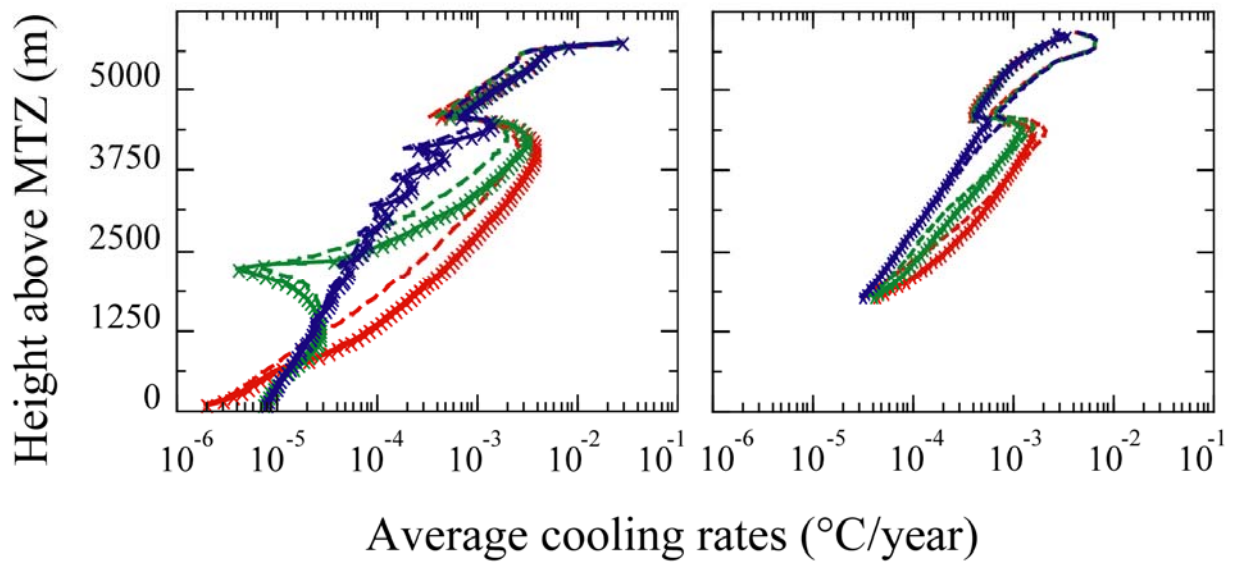
Figure 4: Same as Fig. 3 for a hydrothermal cracking temperature $T_{crac} = 1000^{\circ}\text{C}$.



781
 782
 783
 784
 785
 786
 787
 788
 789

Figure 5: Thermal history of the gabbro versus their final height above MTZ in the cooled lower crust and the G (top panels), M (middle) and S (bottom) crustal accretion modes. Left panels display the $T(t)$ evolution of lagrangian tracers along their trajectories in the lower crust; Middle panels give this temperature evolution for different depths (given in height above MTZ in panels); Evolutions of the instantaneous cooling rates are given in the right panels. The results have been obtained with $T_{crac} = 700^{\circ}\text{C}$.

790



791
 792 *Figure 6: Average cooling rates (ACR) calculated from Eq. 15 using two*
 793 *temperature intervals. The first, from 1275 to 1125 $^{\circ}\text{C}$, covers most of our crystallization*
 794 *range (left panel) the second, from 1050 to 850 $^{\circ}\text{C}$ involves mainly sub-solidus*
 795 *temperatures (right panel). The vertical coordinate corresponds to the final depths reached*
 796 *by the tracers at the end of computation. ACR curves are drawn for the G (red curves), M*
 797 *(green curves) and S (blue curves) crustal accretion modes. In each panel, heavy solid*
 798 *lines correspond to cases with two orders of magnitude viscosity contrasts and high*
 799 *cracking temperature (1000 $^{\circ}\text{C}$). The cases obtained by changing the viscosity contrasts*
 800 *superimpose perfectly (X symbols). Finally, the results obtained with an intermediate*
 801 *hydrothermal cracking temperature of 700 $^{\circ}\text{C}$ are displayed with dashed line.*
 802